creative commons
COMMONS DEED

저작자표시-비영리-변경금지 2.0 대한민국

이용자는 아래의 조건을 따르는 경우에 한하여 자유롭게

- 이 저작물을 복제, 배포, 전송, 전시, 공연 및 방송할 수 있습니다.

다음과 같은 조건을 따라야 합니다:

저작자표시. 귀하는 원저작자를 표시하여야 합니다.

비영리. 귀하는 이 저작물을 영리 목적으로 이용할 수 없습니다.

변경금지. 귀하는 이 저작물을 개작, 변형 또는 가공할 수 없습니다.

- 귀하는, 이 저작물의 재이용이나 배포의 경우, 이 저작물에 적용된 이용허락조건을 명확하게 나타내어야 합니다.
- 저작권자로부터 별도의 허가를 받으면 이러한 조건들은 적용되지 않습니다.

저작권법에 따른 이용자의 권리는 위의 내용에 의하여 영향을 받지 않습니다.

이것은 이용허락규약(Legal Code)을 이해하기 쉽게 요약한 것입니다.

Disclaimer

dCollection

공학박사 학위논문

Extreme miniaturization of optical devices using multi-layered metasurfaces

적층형 메타표면을 이용한 광소자의 초소형화

2019년 2월

서울대학교 대학원
전기·정보공학부

윤정근

Extreme miniaturization of optical devices using multi-layered metasurfaces

지도 교수 이병호

이 논문을 공학박사 학위논문으로 제출함

2019년 2월

서울대학교 대학원
전기·정보공학부

윤정근

윤정근의 공학박사 학위논문을 인준함
2019년 2월

위 원 장 _____(인)

부위원장 _____(인)

위 원 _____(인)

위 원 _____(인)

위 원 _____(인)

Abstract

Extreme miniaturization of optical devices using multi-layered metasurfaces

Jeong-Geun Yun

Department of Electrical and Computer Engineering

College of Engineering

Seoul National University

The evolution of artificial intelligence and communication technologies have enabled to provide various technological devices in a form that is accessible anytime and anywhere. Thus, this trend requires the convergence of various complicated optical devices. However, not only the bulky size but also the difficulties in the integration of the conventional optical components such as polarizers, spatial light modulators, and optical mirrors are significant obstacles in developing the mobile optical devices.

In order to overcome the limitations of conventional optical devices, the development of compact optical devices using metamaterials and metasurfaces has been actively studied. However, the weak light-matter interaction of the metasurface and the complex fabrication process of the metamaterials hinder to develop practical optical systems.

In this dissertation, the miniaturized various optical devices are demonstrated using the multi-layered metasurfaces that are achieved by stacking multiple metasurfaces with subwavelength distances among the layers. Compared with the single layer of metasurface, the multi-layered metasurfaces can enhance the light-matter interaction and combine multiple functions through allowing additional degrees of freedom to manipulate the light. Moreover, it can be a promising solution for practical applications because the fabrication is relatively easier than the three-dimensional metamaterials. Therefore, in this dissertation, novel optical devices

that combine the multiple roles of various optical elements within subwavelength scales are demonstrated using the multi-layered metasurfaces.

Firstly, a novel optical device capable of independently controlling the amplitude and polarization angle of the transmitted light is proposed. The proposed structure consists of anisotropic nanorods and grating layers. The nanorods serve to rotate the polarization of light according to the rotated angle of their axes, and the grating layer acts as a linear polarizer. The polarization rotation angle of the transmitted light is determined by the rotated angle of the grating structure, and the final transmittance is determined by controlling the rotated angle of the nanorods. Thus, the proposed structure can transmit linearly polarized light with an arbitrary polarization angle and amplitude when unpolarized light is incident. The proposed structure is expected to be applicable to various optical devices because the function of polarization rotator and amplitude modulator can be realized with thickness of several hundred nanometers.

Secondly, ultracompact color pixels that can express high color depth with wide gamut have been proposed. The proposed structure can be understood as a structure that mimics the combined structure of a polarizer, a color filter, and a liquid crystal in liquid crystal display. The proposed structure is achieved by stacking grating layer on the rotated nanorod metasurface. Each nanorod works as a polarization rotator only at a specific resonance wavelength determined by the Mie resonances of the nanorods. Therefore, when white light polarized parallel to the grating axis is incident on the proposed structure, only the specific spectral response can be transmitted through the polarization rotation. Thus, the spectral resonance (resonance wavelength and bandwidth) and the intensity of the transmitted light can be independently controlled by the size and the rotated angle of the nanorods, respectively. Also, the cavity effect originating from the metasurface layers permits an additional degree of freedom for manipulating the Mie resonances, and thus this effect is exploited to generate pure colors. The proposed structure is expected to be applicable to next-generation display devices because it has advantages of thin thickness and very small pixel size.

Finally, an ultrathin circular polarizer capable of operating over the entire visible light is implemented by the helically stacked metal nanogratings. The proposed structure transmits the circularly polarized light rotating in the opposite direction to that of the structure, but it reflects the light rotating in the same direction. In this configuration, the nanograting structures are not linear polarizers but anisotropic current sheets. The nanograting layers induce the electrical currents along the axis

of each layer, which results in the non-resonant three dimensional chiral loop. The proposed structure with a thin thickness is expected to be useful for miniaturization of various optical devices by replacing the conventional circular polarizers having narrow bandwidth and bulky size.
This dissertation is expected to contribute to the miniaturization of existing optical elements by developing ultrathin optical elements and multifunctional optical devices with a small form factor.

Keyword: Amplitude modulation, Color generation, Metasurface, Multi-layered structure, Polarization control, Subwavelength structure.
Student Number: 2015-30199

Contents

Abstract ..... **i**

Contents ..... **iv**

List of Figures ..... **vi**

Chapter 1. Introduction **1**

1.1 Backgrounds 1

1.2 Motivation and purpose of this dissertation 4

1.3 Organization of this dissertation 9

Chapter 2. Spatial light modulation of polarization and amplitude over broad bandwidth using multi-layered anisotropic metasurfaces **11**

2.1 Introduction 11

2.2 Polarization rotation in multi-layered anisotropic metasurfaces 14

2.2.1 Polarization rotation in bi-layered anisotropic metasurfaces 14

2.2.2 Broadband nondispersive optical rotator using tri-layered metasurfaces 23

2.3 Simultaneous control of polarization and amplitude using multi-layered metasurfaces 29

2.4 Conclusion 34

Chapter 3. Ultracompact meta-pixels for true color generation using bi-layered hybrid metasurfaces **37**

3.1 Introduction 37

3.2 Principles of the spectral modulation using the bi-layered hybrid metasurfaces 40

3.3 Independent control of the spectral resonance and intensity using the bi-layered hybrid metasurfaces 51

3.4 Meta-pixels for high color depth generation 56

3.4.1 Concept of the meta-pixels based on additive color mixing method 56

3.4.2 Gradual tuning of the response colors using the meta-pixels 58

3.5 Fabrication and optical measurement 61

3.5.1 Fabrication process 61

3.5.2 Optical measurement 64
3.6 Discussion & Conclusion 67
3.6.1 Reflection type structures 67
3.6.2 Conclusion 68
Chapter 4. Broadband ultrathin circular polarizer using helically stacked nanogratings 70
4.1 Introduction 70
4.2 Circular polarizer using helically stacked nanogratings 74
4.2.1 Basic principle 74
4.2.2 Non-resonant characteristic of helically stacked nanogratings 75
4.2.3 The helically stacked multiple nanograting layers 82
4.3 Experimental demonstrations 87
4.4 Discussion & Conclusion 91
4.4.1 For various optical systems 91
4.4.2 Conclusion 92
Chapter 5. Conclusion 94
Bibliography 97
Appendix 102
초 록 103

List of Figures

Figure 1.1 Schematic illustration of the multi-layered metasurfaces (left) and the additional physical phenomena originating from the multiple layers (right). 4

Figure 1.2 Schematic illustrations of the miniaturized optical devices using the multi-layered metasurfaces, which are proposed in this dissertation. (a) Spatial light modulation of amplitude and polarization angle. (b) Ultracompact color pixel with high color depth and wide gamut. (c) Ultrathin circular polarizer with broadband width. 5

Figure 2.1 An artistic illustration of the bi-layered anisotropic metasurface and (b) its unit cell structure. The Al nanograting, the first layer, is aligned along the *y*-axis and has a period = 150 nm, width = 40 nm and thickness = 100 nm. The Al nanorods, which have a period = 300 nm, width = 85 nm, length = 290 nm and thickness = 70 nm, are stacked on the nanograting with separation d and twisted angle θ. 14

Figure 2.2 Cross-sectional schematic illustration of the proposed bi-layered structure for *x*-polarized incident light. 16

Figure 2.3 (a) For *x*-polarized incidence, the transmission spectra of co- (black solid line) and cross-polarization components (black dotted line) and rotation angle φ (gray solid line) of the proposed structure, with $\theta = 45°$ and $d = 50$ nm. (b) The phase difference between the transmitted *x*- and *y*-polarized light (black solid line) and DoLP (gray solid line). The shaded region refers to the operating bandwidth that ensures high quality linearly polarized light. 18

Figure 2.4 The electric field distributions of *x*-polarized (left) and *y*-polarized light (right) in the *x*-*z* plane for *x*-polarized incident light with wavelength of 1000 nm. The grating and the nanorod are indicated by black solid lines. 20

Figure 2.5 For *x*-polarized incident light, (a) rotation angle φ and (b) total transmission of the bi-layered anisotropic metasurface while varying the twisted angle of the nanorod θ. (c) Rotation angle φ and (d) total transmission of the bi-layered anisotropic metasurface for varying d. 21

Figure 2.6 Schematic illustrations for the tri-layered anisotropic metasurface. The nanorod layer and upper grating layer are twisted θ_1 and θ_2 with respect to the lower grating layer, respectively. 23

Figure 2.7 The transmission spectra and DoLP of the tri-layered metasurface with $\theta_1 = 45°$, $\theta_2 = 90°$ and d =50 nm for x-polarized incident light..... 25
Figure 2.8 (a) Rotation angle φ and (e) total transmission of the tri-layered structures for varying θ_2..... 26
Figure 2.9 (a) Transmission spectra of the tri-layered structure having various grating periods of 300 nm (black) and 150 nm (gray) with same filling factor (width of the gratings are 80 nm and 40 nm, respectively). The inset shows the electric field distribution (at 550 nm) of the tri-layered structure having P_g = 300 nm. (b) The transmission spectra of the tri-layered structure having various nanorod periods of 450 nm (black) and 300 nm (red) with same filling factor (width/length of the nanorods are 120nm/435nm and 80nm/290nm, respectively)..... 27
Figure 2.10 (a) A schematic illustration of the polarization-amplitude modulators based on multi-layered metasurface simultaneously generating an arbitrary amplitude and rotation angle φ. (b) The magnification of the proposed structure. The Al nanograting layers have a period = 150 nm, width = 40 nm and thickness = 100 nm. The Al nanorods have a period = 300 nm, width = 85 nm, length = 290 nm and thickness = 70 nm. Each layer is sequentially stacked with separation = 50 nm. The nanorod and top nanograting layer are twisted by θ_1 and θ_2 with respect to the bottom nanograting layer, respectively. The amplitude and optical rotation angle are modulated by θ_1 and θ_2, respectively**.**..... 29
Figure 2.11 Electric field distributions of the multi-layered structures with various θ_1 and θ_2 are presented. The insets indicate the top view of the multi-layered structures with the bottom grating (blue), the nanorods (purple), and the upper grating (red). (a) $\theta_1 = 15°$, $\theta_2 = 30°$, (b) $\theta_1 = 65°$, $\theta_2 = 30°$, (c) $\theta_1 = 90°$, $\theta_2 = 30°$, (d) $\theta_1 = 30°$, $\theta_2 = 60°$, (e) $\theta_1 = 60°$, $\theta_2 = 60°$, (f) $\theta_1 = 90°$, $\theta_2 = 60°$, (g) $\theta_1 = 45°$, $\theta_2 = 90°$, (h) $\theta_1 = 65°$, $\theta_2 = 90°$, (i) $\theta_1 = 80°$, $\theta_2 = 90°$..... 31
Figure 2.12 Transmission spectra obtained for the polarization–amplitude modulators with (a) $\theta_2 = 30°$, (b) $\theta_2 = 60°$, and (c) $\theta_2 = 90°$ while varying θ_1. The white dashed lines indicate the condition, $\theta_1 = \theta_2/2$.Rotation angle φ of the polarization–amplitude modulators with (d) $\theta_2 = 30°$, (e) $\theta_2 = 60°$, and (f) $\theta_2 = 90°$ while varying θ_1**.**..... 33
Figure 3.1 (a) Artistic rendering of the bi-layered hybrid metasurface. (b) Unit cell structure of the proposed structure. The period, thickness, and width of the nanograting are 125 nm, 40 nm, and 120 nm, respectively. (c) The unit cell structure on the y-z plane. The x-

polarized light is incident on the rod side. 40
Figure 3.2 Schematic demonstration of the independent control of the spectral intensity and wavelength. The intensity and wavelength of the transmitted light can be controlled by the rotated angle (θ) and size (w, l) of the nanorods, respectively. 44
Figure 3.3 Transmittance spectra of the bi-layered hybrid metasurfaces having various nanorods of (a) w = 30 nm, l = 80 nm, (b) w = 60 nm, l = 90 nm, (c) w = 100 nm, l = 120 nm and fixed θ = 45° as changing d..... 45
Figure 3.4 (a) The transmittance spectra of the various structures with w = 100 nm, l = 120 nm, and θ = 45°. For x-polarized incidence light, the transmitted y-polarized light of the nanorod layer without the nanograting (black line) and the transmittance of the bi-layered structures varying d (color lines) are calculated. (b) The electric distributions of various structures represented as R_1, R_2, and R_3 in Fig. 2(e). The R_1 and R_3 have the nanograting layer with d = 150 nm and 100 nm, respectively, and R_2 does not have the nanograting layer. 47
Figure 3.5 (a) Calculated CIE chromaticity diagrams of the bi-layered hybrid metasurfaces as changing w and l. The distance d and the rotated angle of the nanorods θ are set to 170 nm and 45°, respectively. The bi-layered structures with the highest purity RGB colors are indicated by white solid stars. Each RGB structure has various size of w = 30 nm, l = 50 nm (blue), w = 60 nm, l = 90 nm (green), w = 110 nm, l = 120 nm (red). (b) The area of the RGB color space of the bi-layered structures with various d. 48
Figure 3.6 Calculated CIE chromaticity diagrams of the nanorod layers without the nanograting as changing w and l..... 50
Figure 3.7 The cross-sectional (left) and the top view (right) SEM images of the fabricated bi-layered hybrid metasurface sample. 51
Figure 3.8 (a) Captured images of the transmitted light from the fabricated bi-layered hybrid metasurfaces with θ = 45° and various w and l. (b) Transmittance spectra of the fabricated samples (S1 – S8) and (c) the spectra normalized by the intensity of the source LED. 52
Figure 3.9 CIE chromaticity diagrams of the simulation (a) and experimental results (b). The simulation results are calculated for the proposed structures with various size (w = 30 ~ 110 nm and l = w + 10 ~ 120 nm) at θ = 45° and d = 170 nm. 54
Figure 3.10 Captured images of the transmitted lights from the fabricated bi-layered

structures with varying θ while keeping (a) w = 45 nm, l = 90, (b) w = 60, l = 100, (c) w = 120, l = 180. Transmittance spectra of the fabricated samples with (d) w = 45 nm, l = 90, (e) w = 60, l = 100, (f) w = 120, l = 180. 55
Figure 3.11 Schematic illustration of supercell structure of the proposed meta-pixel. For simplicity, the nanogorating layer is omitted in this illustration. 56
Figure 3.12 Schematic illustration of the supercell structures of the 1 × 2 meta-pixel with orange and green sub-pixels (left), and the image of the transmitted light from the fabricated meta-pixel sample (right). The rotated angle of the orange sub-pixel is fixed at 45°, and the rotated angle of the green sub-pixel (θ_g) changes from 0° to 45°. 58
Figure 3.13 Experimentally measured (a) Transmittance spectra and (d) color space of the meta-pixel sample divided by five areas (A1 – A5) 59
Figure 3.14 Fabrication flow chart for the bi-layered hybrid metasurfaces. 61
Figure 3.15 Flow chart for aligning the multi-layered structures. 63
Figure 3.16 The experimentally measured spectrum of the input LED source. 64
Figure 3.17 (a) Captured images of the transmitted light from the fabricated bi-layered hybrid metasurfaces with θ = 45° and various w and l, without the polarizer parallel to the grating axis. (b) Transmittance spectra of the blue color pixel (blue line) and single grating layer (black line) with an additional polarizer. (c) The captured images of the transmitted light from the color pixel (left) and the single grating layer (right) with an additional polarizer. 66
Figure 3.18 (a) Schematic illustrations of the reflection type color pixel structures. (b) CIE diagrams of reflected y-polarized lights of the reflection type structures varying sizes (w, l) of the nanorods. The reflection spectra of x-polarized light from the structures with (c) w = 50 nm, l = 110 nm, (d) w = 80 nm, l = 120 nm as changing the rotated angle of the nanorods. 67
Figure 4.1 (a) Schematic illustrations of the proposed helically stacked Al nano-grating structure for visible wavelength ranges. (b) The magnified schematic of the double-layered Al nano-grating structure. The nano-gratings have period (p), width (w) and thickness (t), and they are helically stacked with twisted angle (θ) and separation (d). 74
Figure 4.2 (a) Transmission of Al nanorod array for the LP light and (b) helically stacked nanorod array for the CP lights. The nanorods have p = 150 nm, l = 100 nm, w = t = 30 nm. The bottom nanorods are parralel to y-axis, and the upper nanorods are helically stacked

with d = 50 nm and θ = 45°. (c) Transmission of Al nano-gratings for the LP light and (d) helically stacked nano-gratings for the CP lights (d) with p = 150 nm, $w = t$ = 30 nm, d = 50 nm and θ = 45°. 75

Figure 4.3 Extinction ratio (T_{RCP}/T_{LCP}) and operting bandwidth of the stacked nanorod (black) and nano-grating (gray). 79

Figure 4.4 Electric current distribution in the helically stacked Al nanorods (a) for LCP incident light at 508 nm and (b) RCP incident light at 653 nm. Electric current distribution in the helically stacked Al nano-grating for (c) LCP and (d) RCP incident light at 609 nm. The white arrows indicate the direction of the induced current. 80

Figure 4.5 Transmission curves and *ER* for CP light as changing the number of the helically stacked nano-grating layers. The structures are constructed with left handed manner, and structure parameters are p = 150 nm, $w = t$ = 30 nm, d = 30 nm and θ = 45°. 82

Figure 4.6 Transmission spectra of the 7-layered structures varying d for (a) RCP and (b) LCP incident light 84

Figure 4.7 Averaged extinction ratio (T_{RCP}/T_{LCP}) and (b) averaged transmission for RCP light of the four-layered Al nano-grating structure over the wavelength ranges from 400 nm to 700 nm as a function of d and θ. (c) The averaged extinction ratio and (d) averaged transmission for RCP light of the four-layered Al nano-grating structure with fixed d = 30 nm and θ = 45° as a function of t and fill factor. 85

Figure 4.8 (a) Flow chart of the fabrication process for helically stacked nanograting layers. (b) Cross-sectional SEM images of the fabricated sample. 87

Figure 4.9 (a) The captured CCD images from the fabricated sample at 532 nm, 660 nm, and 980 nm. The left figure is for RCP incident light and the right one for LCP incident light. (b) The output intensity of the RCP light (black) and LCP light (red) along the red line in Fig. 4.8(a) is shown. 89

Figure 4.10 Transmission curves for (a) the helically stacked gold nano-grating and (b) the helically stacked silver nano-grating. The structures are helically stacked with the four layers of the nano-gratings as shown in the inset of Fig. 4.5(c), and the structure parameters are p = 150 nm, $w = t$ = 30 nm, d = 30 nm and θ = 45°. 92

Chapter 1. Introduction

1.1 Backgrounds

The development of information and communication technology has inspired huge changes in various areas in modern society. People can use mobile devices to create and send massive information anytime, anywhere. Nowadays, the 4th industrial revolution is emerging from the technical convergences, and thus many countries are making a lot of effort to prepare this new paradigm. To successfully take a leading position in the revolution, it is very important not only to make massive software platforms for generating information, but also to develop high-tech hardware to address the massive information. Thus, the next generation information devices are required to have multiple functions to sense, process, and communicate the surrounding information. Therefore, the development of multi-functional devices through integrating various devices within a small form factor becomes a key issue for the next-generation technologies.

Optics has been treated as a crucial technology in many fields because the light can provide people and devices with the opportunities to receive and transmit vast information. For examples, sensors can collect information, and the optical communication allows the interaction among the devices, and displays are the best means for transferring information to people. In other words, optics plays a

significant role in connecting the surrounding environment, devices, and human. Despite this powerful potential, there are crucial limitations in developing complex and compact optical devices. Conventional optical components such as a polarizer, spatial light modulators, and lenses are difficult to miniaturize their volume and integrate with each other. This limitation originates from the diffraction limit, an inherent property of light, which makes it impossible to squeeze light into the structure smaller than the wavelength of the light. Thus, miniaturization of optical devices has caused a bottle-neck in most of the mobile optical devices.

Recently, metamaterials and metasurfaces have been received great attentions for promising solutions to develop the miniaturized optical devices. Metamaterials that are artificially engineered three-dimensional (3D) periodic structures enable to control the light, even in the manner that does not exist in nature [1-3]. Also, metasurfaces are two-dimensional (2D) periodic structures with subwavelength scales [4]. Various optical elements such as polarizers [5,6], complex modulators [7], lenses [8,9] have been realized through the magnificent light modulation abilities of the metamaterials and metasurfaces. However, there are several difficulties for the metamaterials and metasurfaces to become practical optical devices. The metamaterials are fabricated by the complex processes such as direct laser writing, and micro-electromechanical fabrication methods. Moreover, in the case of 3D metallic metamaterials, the materials and substrates of the structures are limited because the electrochemical deposition method

requires conductive substrate such as indium-tin-oxide coated substrate and because only certain metals such as gold, silver, and tungsten [10] can be deposited by the method. Furthermore, it makes difficult for the single layer of metasurfaces to develop multi-functional devices because they exhibit relatively weak light-matter interaction and the limited degree of freedom. Thus, to overcome these limitations, multi-layered metasurfaces have been studied [11].

1.2 Motivation and purpose of this dissertation

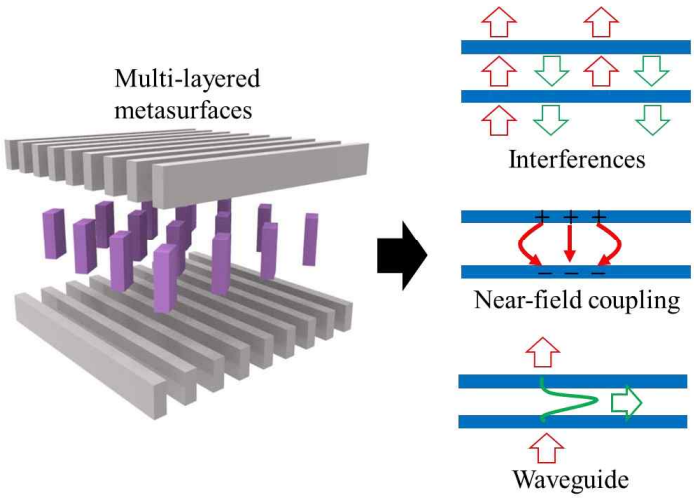

Figure 1.1 Schematic illustration of the multi-layered metasurfaces (left) and the additional physical phenomena originating from the multiple layers (right).

Figure 1.1 shows the schematic illustration of the multi-layered metasurfaces which are realized by multiple metasurface layers through sequentially stacking the layers with a subwavelength distance. Compared with the 3D metamaterials, the multi-layered metasurfaces can be easily fabricated by multiple lithography method. The multi-layered metasurfaces can support stronger light-matter interaction than the single layer of metasurfaces through additional physical effects such as near-field coupling, wave guide effect, and interferences among the lights. Thus, these physical effects can be additional options to manipulate the light and provide high degree of freedom. Furthermore,

the physical results of the multi-layered metasurfaces can be intuitively deduced from the physical effects of the individual single layer metasurfaces. Thus, this insight could be a tremendous help for developing versatile optical devices.

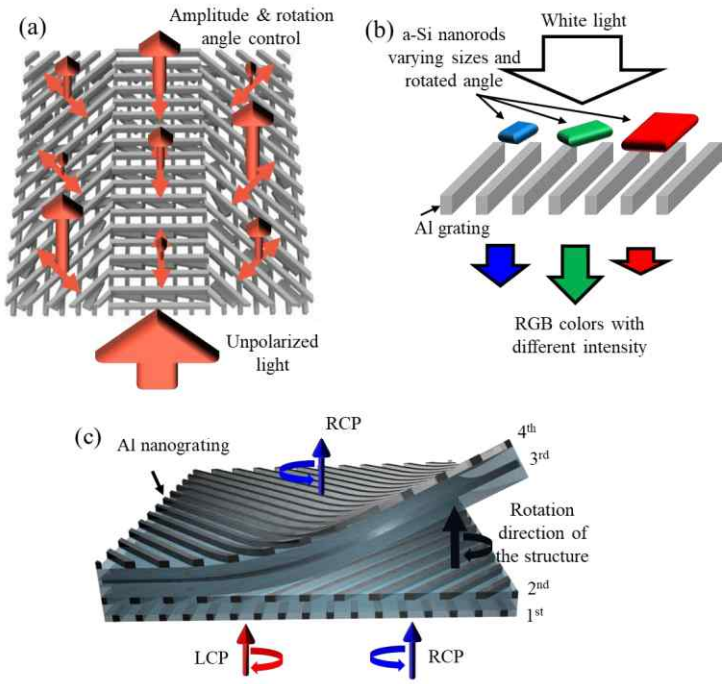

Figure 1.2 Schematic illustrations of the miniaturized optical devices using the multi-layered metasurfaces, which are proposed in this dissertation. (a) Spatial light modulation of amplitude and polarization angle. (b) Ultracompact color pixel with high color depth and wide gamut. (c) Ultrathin circular polarizer with broad bandwidth.

In this dissertation, the miniaturized optical devices using multi-layered metasurfaces is the main purpose. It also includes the

development of novel optical devices which enable to provide multiple functions within subwavelength scales. To achieve the purpose, the multi-layered metasurfaces that are composed of multiple metasurfaces with various geometric configurations and materials are exploited. The role of the individual single metasurface layers are studied, and then the novel effects originating from the interaction among the layers are also investigated to develop the miniaturized optical devices. In this dissertation, three of the miniaturized optical devices are proposed using multi-layered metasurfaces.

Firstly, a novel structure that can independently control the amplitude and polarization angle of the transmitted linearly polarized (LP) light is proposed by stacking several metallic metasurfaces as shown in Fig. 1.2(a). The proposed device consists of anisotropic nanorods serving to rotate the polarization of light depending on the rotated angle of their axes, and the grating layers acting as linear polarizers. Each layer is sequentially stacked with each rotated angle. The rotation angle of the transmitted light is determined by the rotated angle of the grating layer, and the transmittance is controlled by adjusting the rotated angle of the nanorods. Thus, the proposed structure transmits LP light with an arbitrary polarization angle and amplitude when unpolarized light is incident. The proposed structure is expected to be applicable to various optical devices because the function of polarization rotator and amplitude modulator can be realized with thickness of several hundred nanometers.

Secondly, ultracompact color pixels that can express various colors

with high color depth and wide gamut are demonstrated using the multi-layered metasurfaces as shown in Fig. 1.2(b). The independent control of the resonance wavelength and intensity of the transmitted light can be realized by adjusting different geometric parameters. The proposed structure can be understood as a structure in which a polarizer, a color filter, and a liquid crystal of a conventional liquid crystal display are combined. The proposed structure is achieved by stacking the metal grating layer on the dielectric nanorod metasurface. When white light polarized parallel to the axis of the grating layer is incident, only the specific spectral resonance which is determined by the interferences among the Mie resonances in the nanorods can pass through the grating layer. At that time, the intensity of the transmitted light is related to the rotated angle of the nanorods because the nanorods can rotate the incident light depending on the rotated angle. Moreover, the cavity effect between the layer can provide an additional degree of freedom for manipulating the interferences, and thus this is exploited to obtain pure colors. In addition, a method for realizing ultracompact color pixels with high color depth is proposed using the multi-layered structures. The proposed structure is expected to be applicable to next-generation display devices because color pixels having high color depth and wide gamut can be realized within thin thickness and very small pixel size.

Finally, an ultrathin circular polarizer operating over the entire visible wavelengths is implemented by the helically stacked metal nanograting layers. Here, the nanograting layer is anisotropic current sheets

inducing electric current along the axis of the nanograting rather than a linear polarizer. When the light rotating in the opposite direction to that of the structure is incident on the structure, it feels the structures nearly transparent. In contrast, for the incident light rotating in the same direction, it reflects the light. In the proposed structure, the non-resonant chiral current loop that is formed in the helically stacked structure allows to make it operable in a wide bandwidth. The proposed structure is expected to be useful for miniaturization of various optical devices by replacing the conventional circular polarizers which have been suffered from narrow bandwidth and bulky volumes.

1.3 Organization of this dissertation

This dissertation proposes several optical devices using multi-layered metasurfaces.

In Chapter 2, spatial light modulation of amplitude and polarization rotation is demonstrated by multi-layered metasurfaces. In section 2.1, the principle of the polarization rotation in the proposed structure is explained with numerical simulations and analytic equations. In section 2.2, it is numerically explained that the amplitude of the transmitted light is controlled. Finally, the conclusion and brief discussion are presented in section 2.4.

In Chapter 3, ultracompact color pixels that can provide high color depth and wide gamut are presented. The principle of independent control of spectral resonance and intensity of the transmitted light is theoretically demonstrated in section 3.2. The section 3.3 accounts for the independent control with experimental results and simulations. In section 3.4, the scheme for high color generation using the proposed structures is proposed based on additive color mixing method. Also, the concept is experimentally verified. In section 3.5, the fabrication process and optical measurement for the multi-layered metasurfaces are elucidated. In section 3.6, the conclusion and brief discussion for application to practical display systems are explained.

In Chapter 4, an ultrathin circular polarizer is proposed using helically stacked nanograting layers. In section 4.2, the principles of the proposed structure are theoretically explained and verified by

simulation results. In section 4.3, the fabrication process is addressed, and the proposed structure is experimentally verified by the fabrication samples. The section 4.4 provides conclusion and discusses the improvement to apply to practical devices.

In Chapter 5, a summary of this dissertation is presented, and perspectives of the proposed structures are discussed.

Chapter 2. Spatial light modulation of polarization and amplitude over broad bandwidth using multi-layered anisotropic metasurfaces

2.1 Introduction

Polarization and amplitude of electromagnetic waves are fundamental properties that can be used to manipulate the manner of light-matter interactions. Thus, controlling the polarization state and amplitude of light is essential in complex and multifunctional optical applications such as optical communication, chemistry, biology, and diffractive optics [12-15]. Conventional methods for manipulating polarization states are implemented using multiple optical elements such as polarizers, waveplates, liquid crystals, and magneto-optical crystals. However, their weak light-matter interaction and highly dispersive optical activity result in a narrow bandwidth and bulky configurations. In addition, multiple optical components are required to control the polarization and amplitude simultaneously, which is a bottleneck in the miniaturization of optical information processing systems.

Metasurfaces are arrays of nanoantennae and serve as promising

solutions for engineering optical properties within a subwavelength thickness. It is possible to use metasurfaces to manipulate the complex amplitude and polarization of transmitted light in a subwavelength thickness. Hence, many flat optical devices based on metasurfaces such as polarizers [16], waveplates [17,18], and meta-holograms [19] have been studied. Recently, optical rotators that can rotate the polarization plane of linearly polarized (LP) light have been demonstrated using metasurfaces for various wavelengths [20-23]. However, the transmission-type rotators suffer from problems of a narrow bandwidth and dispersive optical activity, and their application is limited due to their low transmission and modulation depth. Therefore, it has been an ongoing challenge to realize large and nondispersive optical activity with high transmittance over a broad wavelength range. Furthermore, to the best of author's knowledge, nanophotonic devices that enable the simultaneous control of polarization and amplitude have not yet been reported.

Here, we propose a transmission-type polarization-amplitude modulator that can independently control the polarization and amplitude of the transmitted light simultaneously using multi-layered anisotropic metasurfaces (grating-nanorod-grating layers). This simultaneous control is accomplished by the phenomenon that the rotation of the polarization plane and amplitude of the transmitted light are determined by the distinct geometric parameters of the metasurface layers. First, the upper grating layer determines polarization rotation that can pass through it.

Next, the nanorod layer controls the amount of polarization conversion and serves to align the polarization rotation to the upper grating layer. This scheme is different from the stacking three subwavelength wiregrid polarizers that provides polarization rotation. Also, the staking three wire polarizer is not a suitable approach to realize independent control of polarization and amplitude. That is because the wire grid polarizers, in contrast to the nanorod layer, do not serve to align the polarization rotation to the upper grating layer but serve to align the polarization rotation to their rotation angles. Broadband polarization rotation with an arbitrary angle and high transmission over a broad wavelength range is demonstrated numerically for multi-layered metasurfaces. High transmission and nondispersive optical rotation are obtained by Fabry-Pérot-like cavity that originates from the adjacent two anisotropic metasurface layers and improves the light-matter interactions over a broad bandwidth. The proposed structure allows extreme miniaturization of optical systems and can be applied to optical communication, polarization resolved image, and displays. In this section, the proposed structures are theoretically analyzed and numerically verified.

2.2 Polarization rotation in multi-layered anisotropic metasurfaces

2.2.1 Polarization rotation in bi-layered anisotropic metasurfaces

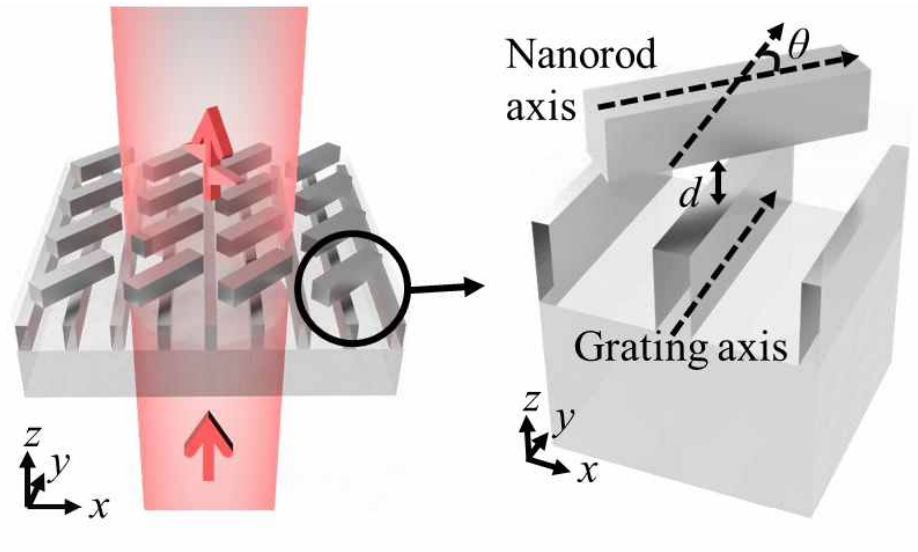

Figure 2.1 An artistic illustration of the bi-layered anisotropic metasurface and (b) its unit cell structure. The Al nanograting, the first layer, is aligned along the *y*-axis and has a period = 150 nm, width = 40 nm and thickness = 100 nm. The Al nanorods, which have a period = 300 nm, width = 85 nm, length = 290 nm and thickness = 70 nm, are stacked on the nanograting with separation *d* and twisted angle θ.

First, a bi-layered anisotropic metasurface is considered. Figures 2.1 shows schematic illustrations for the bi-layered metasurface, which

consists of an aluminum (Al) nanograting and twisted Al nanorods with a twist angle of θ and separation of d.

When the thickness of each metasurface layer is smaller than the wavelength of the incident light, such metasurfaces can be modeled as effective surfaces with averaged transverse polarization currents. Also, when the distances between the multiple layers are large enough to prohibit near-field coupling effect among the layers, the multi-layered metasurface structures can be regarded as a series of ultrathin optical sheets, and thus the transmission and reflection characteristics can be predicted by the Jones vector calculus.

The nanograting acts as a linear polarizer: it is nearly transparent to x-polarized incident light but reflects most of the y-polarized incident light. For the simplicity, the nanograting is assumed to be an ideal linear polarizer, and the transmission and reflection Jones matrices of the nanograting can be expressed as $T_g = \begin{pmatrix} 1 & 0 \\ 0 & 0 \end{pmatrix}$ and $R_g = \begin{pmatrix} 0 & 0 \\ 0 & 1 \end{pmatrix}$. Additionally, the Al nanorod interacts dominantly with the light polarized along the direction parallel to the rod axis and generates a plasmonic resonance, which is determined by geometric parameters of the nanorods [24]. The transmission and reflection Jones matrices of the anisotropic nanorod with θ = 0 can be expressed as $T_r = \begin{pmatrix} t_{xx} & 0 \\ 0 & t_{yy} \end{pmatrix}$ and $R_r = \begin{pmatrix} r_{xx} & 0 \\ 0 & r_{yy} \end{pmatrix}$, respectively [25]. Those for the nanorod twisted by θ can be described by the

following equations,

$$T_r(\theta) = R^{-1} T_r R = \begin{pmatrix} t_{xx}\cos^2\theta + t_{yy}\sin^2\theta & \cos\theta\sin\theta(t_{xx} - t_{yy}) \\ \sin\theta\cos\theta(t_{xx} - t_{yy}) & t_{xx}\sin^2\theta + t_{yy}\cos^2\theta \end{pmatrix}, \quad (2.1)$$

$$R_r(\theta) = R^{-1} R_r R = \begin{pmatrix} r_{xx}\cos^2\theta + r_{yy}\sin^2\theta & \cos\theta\sin\theta(r_{xx} - r_{yy}) \\ \sin\theta\cos\theta(r_{xx} - r_{yy}) & r_{xx}\sin^2\theta + r_{yy}\cos^2\theta \end{pmatrix}, \quad (2.2)$$

where $R = \begin{pmatrix} \cos\theta & \sin\theta \\ -\sin\theta & \cos\theta \end{pmatrix}$ is the rotation matrix.

For the case of bi-layered structure which is composed of the nanograting and twisted nanorods, Fabry-Pérot-like cavity effect that originates from the multiple reflections between the grating and the nanorod is induced only for *y*-polarized light as shown in Fig. 2.2.

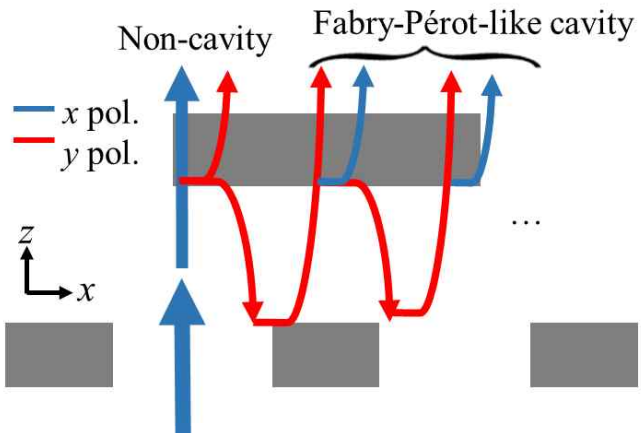

Figure 2.2 Cross-sectional schematic illustration of the proposed bi-layered structure for *x*-polarized incident light.

The total transmission of bi-layered structure is resulted from the superposition of the non-cavity and cavity modes. Thus, it can be expressed via Jones calculus as following equation

$$T_{total}^{bi} = e^{iknd} T_g T_r(\theta) + e^{i3knd} T_g R_r(\theta) R_g T_r(\theta) + e^{i5knd} T_g R_r(\theta) R_g R_r(\theta) R_g T_r(\theta) + \cdots$$

$$= e^{iknd} \begin{pmatrix} t_{xx}\cos^2\theta + t_{yy}\sin^2\theta + e^{i2knd}\sin^2\theta\cos^2\theta(t_{xx}-t_{yy})(r_{xx}-r_{yy}) + \blacksquare\blacksquare\blacksquare 0 \\ \sin\theta\cos\theta[t_{xx}-t_{yy} + e^{i2knd}(r_{xx}-r_{yy})(t_{xx}\sin^2\theta + t_{yy}\cos^2\theta) + \blacksquare\blacksquare\blacksquare 0 \end{pmatrix}. \quad (2.3)$$

Here, k and n are free space wavenumber and refractive index of dielectric spacer between the two layers, respectively. The first term of the equation indicates the transmitted light without the cavity effect, and the other terms represent the light enhanced by Fabry-Pérot-like cavity effect. It is noticeable that the total transmitted light is decided by the interference between the non-cavity and the cavity modes. Also, the cross polarized component (from x- to y-polarized light) implies that the bi-layered structures act as a polarization converter when the nanorod provides anisotropic response that is critically achieved around the plasmonic resonance wavelength of the nanorod. If the separation length d is small enough to make the phase retardation (e^{i2knd}) negligible, the transmitted y-polarized lights can be enhanced over broad wavelengths. Additionally, since the polarization conversion is proportional to $\sin\theta\cos\theta$, it can be controlled by θ. Figure 2.3(a) shows the transmission spectra of the co- and cross-polarizations and optical rotation angle (φ) of the bi-

layered structure when θ = 45° and d = 50 nm for x-polarized incidence. For the numerical simulations, a commercial finite-difference time-domain method tool (Lumerical Solutions, Inc.) is used. Dielectric constants for Al are taken from a textbook [26], and the refractive index of the surrounding environment including substrate and dielectric spacer between the stacked layers is assumed to be 1.5. The rotation angle φ accounts for the rotation of the polarization plane for the LP light. Here, the nanograting and nanorod are designed to work as a linear polarizer and exhibit anisotropic transmission at approximately 1000 nm, respectively.

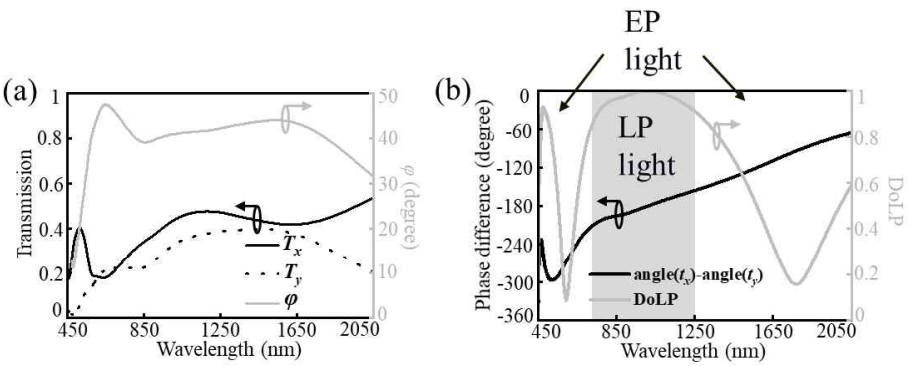

Figure 2.3 (a) For x-polarized incidence, the transmission spectra of co- (black solid line) and cross-polarization components (black dotted line) and rotation angle φ (gray solid line) of the proposed structure, with θ = 45° and d = 50 nm. (b) The phase difference between the transmitted x- and y-polarized light (black solid line) and DoLP (gray solid line). The shaded region refers to the operating bandwidth that ensures high quality linearly polarized light.

Owing to the Fabry-Pérot-like cavity, the polarization conversion to *y*-polarized light is enhanced compared to the single nanorod; thus, a rotation angle of 40 - 47° is achieved over a wide wavelength range (600 - 1850 nm). Since the cross-polarized light experiencing the Fabry-Pérot-like cavity is vulnerable to Ohmic losses of Al, its transmission and optical rotation angle are deteriorated at approximately 800 nm where the interband transition in Al occurs. In spite of this loss, our structure can be a good candidate for highly efficient transmission type polarization generator owing to its large modulation angle with high transmission over 0.8 for a wide bandwidth. Next, to investigate the quality of the transmitted LP light, the phase difference between the transmitted *x*- and *y*- polarized light and the degree of linear polarization (DoLP= $\frac{\sqrt{S_1^2 + S_2^2}}{S_0}$ and S_0, S_1, and S_2 are Stokes parameters) are calculated. As shown in Fig. 2.3(b), the proposed structure shows a wavelength-dependent phase difference. When the DoLP is above 0.9, the transmitted light can be considered as a high-quality LP light. Thus, the transmitted light is nearly LP light from 750 nm to 1260 nm, but it is considered as an elliptically polarized (EP) light at the other wavelengths. Figure 2.4 shows the electric field distributions in the *x*-*z* plane. The incident *x*-polarized light sequentially passes through the nanograting and the nanorod. However, it is apparent that the *y*-polarized light excited from the nanorod cannot

penetrate the nanograting layer and propagates in the +z direction. Based on this field distribution, it can be deduced that our Fabry-Pérot-like cavity works in different manner than does a conventional Fabry-Pérot cavity. The conventional Fabry-Pérot resonator exhibits high electric field confinement between adjacent layers, and thus it provides a highly dispersive transmission spectrum. In contrast, our anisotropic bi-layered metasurface, Fabry-Pérot-like cavity, does not concentrate the electric field inside it. This enables the structure to maintain the enhanced transmission and nondispersive optical rotation angle over a wide bandwidth, as shown in Fig. 2.3(a).

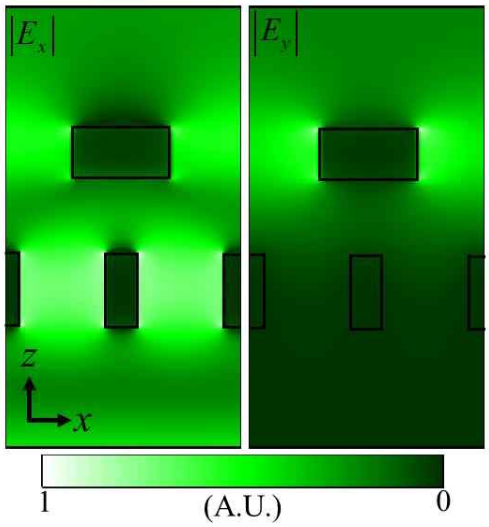

Figure 2.4 The electric field distributions of x-polarized (left) and y-polarized light (right) in the x-z plane for x-polarized incident light with wavelength of 1000 nm. The grating and the nanorod are indicated by black solid lines.

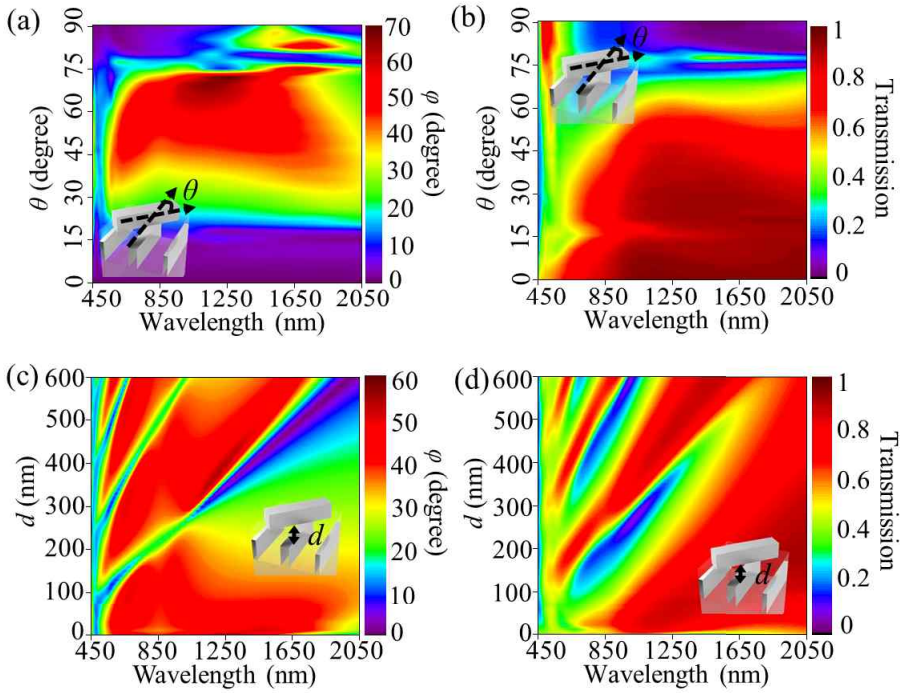

Figure 2.5 For x-polarized incident light, (a) rotation angle φ and (b) total transmission of the bi-layered anisotropic metasurface while varying the twisted angle of the nanorod θ. (c) Rotation angle φ and (d) total transmission of the bi-layered anisotropic metasurface for varying d.

To further understand the underlying mechanisms of the bi-layered structure, the spectra for the total transmission and rotation angle φ are numerically investigated while changing the twist angle of the nanorod θ and separation d. As shown in Figs. 2.5(a) and 2.5(b), it is noticeable that the rotation angle φ increases almost linearly over a wide wavelength range when θ

increases to 70°. Additionally, the total transmission, for $\theta < 45°$, remains over 0.8 in a broad wavelength range, but it drops rapidly after 45°. These facts can be understood from the fact that the transmitted co- and cross-polarized light are adjusted by the twist angle θ (cf. Eqs. (2.1) and (2.2)); the cross-polarized light has a maximum value when θ is 45°, and the co-polarized light is steeply decreased at large θ. In addition, the separation d plays a significant role in the performance of the structure because the distance condition, $2d << 2\pi/k$, should be satisfied to make the phase retardation from the Fabry-Pérot-like cavity negligible. Additionally, when d is too small, the interaction between the adjacent layers becomes strong, and the effect of the higher order Floquet modes must be taken into account, which makes the structure vulnerable to interlayer alignment errors. As shown in Figs. 2.5(c) and 2.5(d), the transmission and rotation dips, due to destructive interference between the non-cavity and cavity modes, are periodically explored for varying d from 100 nm to 600 nm. Additionally, when d is less than 50 nm, transmission fluctuations caused by the interlayer interaction occur. Therefore, the optimal distance d is decided as 50 nm, which is short enough to render the phase retardation negligible.

2.2.2 Broadband nondispersive optical rotator using tri-layered metasurfaces

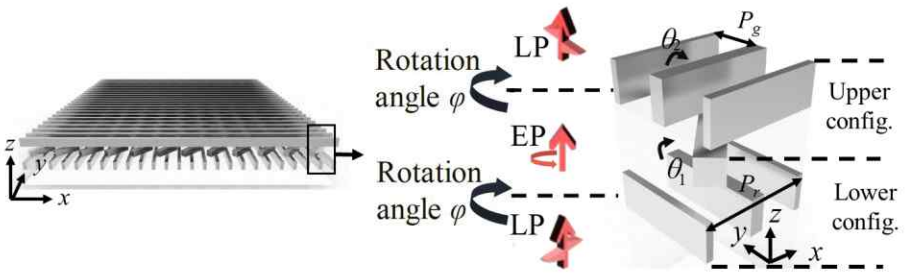

Figure 2.6 Schematic illustrations for the tri-layered anisotropic metasurface. The nanorod layer and upper grating layer are twisted by θ_1 and θ_2 with respect to the lower grating layer, respectively.

In the aforementioned bi-layered structures, the optical rotation angle and operation bandwidth guaranteeing high quality LP light are limited. To eliminate this bandwidth limitation and increase the rotation angle, a tri-layered anisotropic metasurface is considered, which stacks an additional Al nanograting layer, identical to the nanograting in the first layer, on the top of the bi-layered metasurface, as shown in Fig. 2.6. The nanorod layer and upper grating layer are twisted by θ_1 and θ_2 with respect to the lower grating layer, respectively. The tri-layered structure can be considered as a series of two bi-layered metasurfaces. Thus, the transmission Jones matrix of the lower configuration that is composed of the bottom grating and the nanorod layer can be derived by assigning θ_1 to Eq. (2.3), and it is indicated by

$T_{total}^{bi-low} = \begin{pmatrix} e_x(\theta_1) & 0 \\ e_y(\theta_1) & 0 \end{pmatrix} = \begin{pmatrix} e_{1x} & 0 \\ e_{1y} & 0 \end{pmatrix}$. Similarly, the transmission Jones matrix of the upper configuration composed of the nanorod and the top grating layer can be derived by assigning θ_2-θ_1 and transforming Eq. (2.3), and it can be expressed as following equation:

$$T_{total}^{bi-up} = \begin{pmatrix} e_{2x}\cos^2\theta_2 + e_{2y}\cos\theta_2\sin\theta_2 & e_{2x}\cos\theta_2\sin\theta_2 - e_{2y}\cos^2\theta_2 \\ e_{2x}\cos\theta_2\sin\theta_2 + e_{2y}\sin^2\theta_2 & e_{2x}\sin^2\theta_2 - e_{2y}\cos\theta_2\sin\theta_2 \end{pmatrix}, \quad (2.4)$$

where $e_{2x} = e_x(\theta_2\text{-}\theta_1)$ and $e_{2y} = e_y(\theta_2\text{-}\theta_1)$. When the interaction among the metasurface layers can be negligible, the total transmission of the tri-layered structure can be obtained by the product of the transmission matrices of the two bi-layered structures as following equation:

$$T_{total}^{tri} = T_{total}^{bi-up} T_{total}^{bi-low} = \begin{pmatrix} \cos\theta_2[(e_{1x}e_{2x} - e_{1y}e_{2y})\cos\theta_2 + (e_{1x}e_{2y} + e_{2x}e_{1y})\sin\theta_2] & 0 \\ \sin\theta_2[(e_{1x}e_{2x} - e_{1y}e_{2y})\cos\theta_2 + (e_{1x}e_{2y} + e_{2x}e_{1y})\sin\theta_2] & 0 \end{pmatrix}. \quad (2.5)$$

This equation indicates that the transmitted light is, regardless of θ_1, LP light with rotation angle of θ_2 which is perpendicular to the axis of the upper grating layer. In other words, the incident light is converted from LP to EP light while passing through the first and second layers, then the second and third layers convert the EP light to LP light. Also, it is noticeable that $\theta_1 = \theta_2/2$ leads

to $e_{2x} = e_{1x}$ and $e_{2y} = e_{1y}$, and the amplitude of the transmitted light in Eq. (2.5) becomes maximum value.

Figure 2.7 shows the simulation result of the transmitted light waves and DoLP for the tri-layered structure with $\theta_1 = 45°$, $\theta_2 = 90°$, and $d = 50$ nm. The data show an almost unity DoLP and nondispersive optical rotation of 90° over a broad wavelength range (600 nm - 2050 nm) except for short wavelengths where the 150 nm periodic nanograting does not act as a perfect linear polarizer. Moreover, it is easy to understand that the maximum total transmission appears near the resonance wavelength of the nanorod. Based on this scenario, it can be deduced that the operation bandwidth of the multi-layered metasurfaces can be tuned by scaling up and down of the twisted nanorods.

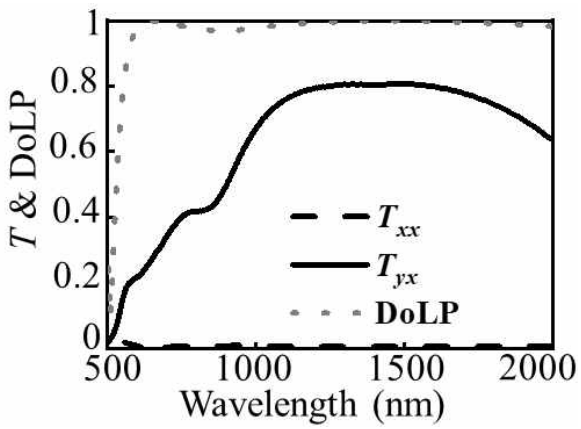

Figure 2.7 The transmission spectra and DoLP of the tri-layered metasurface with $\theta_1 = 45°$, $\theta_2 = 90°$ and $d = 50$ nm for x-polarized incident light.

Figures 2.8(a) and 2.8(b) show the transmission spectra and rotation angle φ for varying θ. It can be seen that φ in the tri-layered structure is determined in the direction perpendicular to the axis of the top nanograting layer and satisfies $\varphi = \theta_2$ which shows a good agreement with the result from Eq. (2.5). Any rotation angle for the polarization plane can be provided by the tri-layered structure as twisting θ_2 from -90° to 90°. This structure also exhibits an additional transmission dip near 1800 nm due to the interlayer interactions, but it shows a high transmission over a broad bandwidth of 600 nm or more.

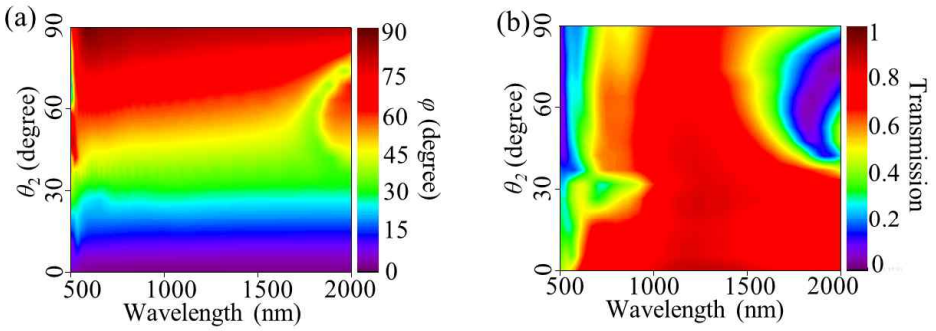

Figure 2.8 (a) Rotation angle φ and (e) total transmission of the tri-layered structures for varying θ_2.

Also, to understand the physical effects of the geometrical parameters of each layer, it is important to understand the design rules of the proposed structures. Firstly, as described above, the operation wavelength can be controlled by the dimensions (period, width, length, thickness) of the nanorod. Secondly, the nanograting layers are designed to act like a linear polarizer for

the operation wavelength range to form the cavity like effect. Based on these design rules, if the period of the nanograting increases, the transmitted light at short wavelengths cannot be controlled by the multi-layered structures.

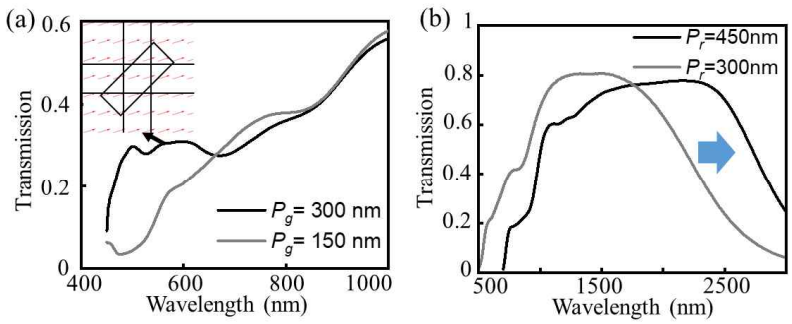

Figure 2.9 (a) Transmission spectra of the tri-layered structure having various grating periods of 300 nm (black) and 150 nm (gray) with same filling factor (width of the gratings are 80 nm and 40 nm, respectively). The inset shows the electric field distribution (at 550 nm) of the tri-layered structure having P_g = 300 nm. (b) The transmission spectra of the tri-layered structure having various nanorod periods of 450 nm (black) and 300 nm (gray) with same filling factor (width/length of the nanorods are 120nm/435nm and 80nm/290nm, respectively).

As shown in Fig. 2.9(a), the non-rotating light leaks at the short wavelength range where the nanograting having P_g = 200 nm does not act like a linear polarizer. Also, when the period of nanorod increases, a red shift of the operation wavelength range occurs as shown in Fig. 2.9(b). Intuitively, theses design rules

indicate that the proposed multi-layered structures have flexibility in the dimensions of the metasurfaces. In this dissertation, the period of the grating is set as P_g = 150 nm to ensure that the nanograting works as a linear polarizer at the short wavelengths (~600 nm), but it is not the unique solution. It is possible that the nanograting layer having P_g = 200 nm is a solution if the width and thickness are carefully designed [27].

2.3 Simultaneous control of polarization and amplitude using multi-layered metasurfaces

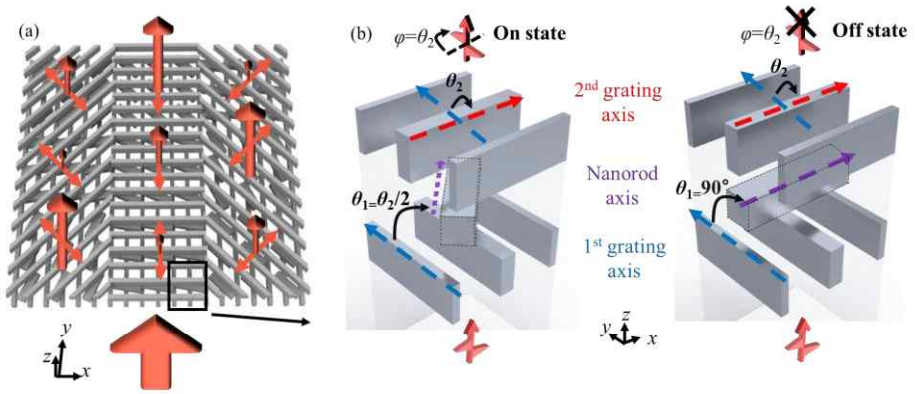

Figure 2.10 (a) A schematic illustration of the polarization-amplitude modulators based on multi-layered metasurface simultaneously generating an arbitrary amplitude and rotation angle φ. (b) The magnification of the proposed structure. The Al nanograting layers have a period = 150 nm, width = 40 nm and thickness = 100 nm. The Al nanorods have a period = 300 nm, width = 85 nm, length = 290 nm and thickness = 70 nm. Each layer is sequentially stacked with separation = 50 nm. The nanorod and top nanograting layer are twisted by θ_1 and θ_2 with respect to the bottom nanograting layer, respectively. The amplitude and optical rotation angle are modulated by θ_1 and θ_2, respectively.

Next, a strategy for simultaneous control of the amplitude and polarization of the transmitted light is demonstrated, as shown in Fig. 2.10. The nanorod and top nanograting layer are twisted by θ_1 and θ_2 with respect to the bottom nanograting layer, respectively. When unpolarized light impinges on the multi-

layered structure from the substrate side, only x-polarized light can pass through the nanograting. Then, the twisted nanorods partially convert the x- to y-polarized light. Finally, the specific light with rotation angle perpendicular to the axis of the upper grating layer can pass through the last layer. Thus, the more light appropriately rotated from the lower two layers, the more light is transmitted through the upper grating layer. Based on this scenario, the proposed multi-layered structure can independently control rotation angle φ and transmitted amplitude by adjusting θ_2 and θ_1, respectively. Here, the θ_1 and θ_2 are assumed to satisfy the following conditions:

$$\begin{cases} \dfrac{\theta_2}{2} \le \theta_1 \le 90° & (0 \le \theta_2), \\ -90° \le \theta_1 \le \dfrac{\theta_2}{2} & (\theta_2 < 0). \end{cases} \tag{2.3}$$

As shown in Fig. 2.10, the proposed structure becomes the “on state” and shows maximum transmission when $\theta_1 = \theta_2/2$ which leads to the rotation angle matching the upper grating layer. The proposed structure becomes the “off state” when θ_1 is 90° which indicates minimum polarization conversion. To investigate the simultaneous control in the multi-layered structure, the electric field distributions at the wavelength of 1000 nm are numerically calculated as shown in Fig. 2.11.

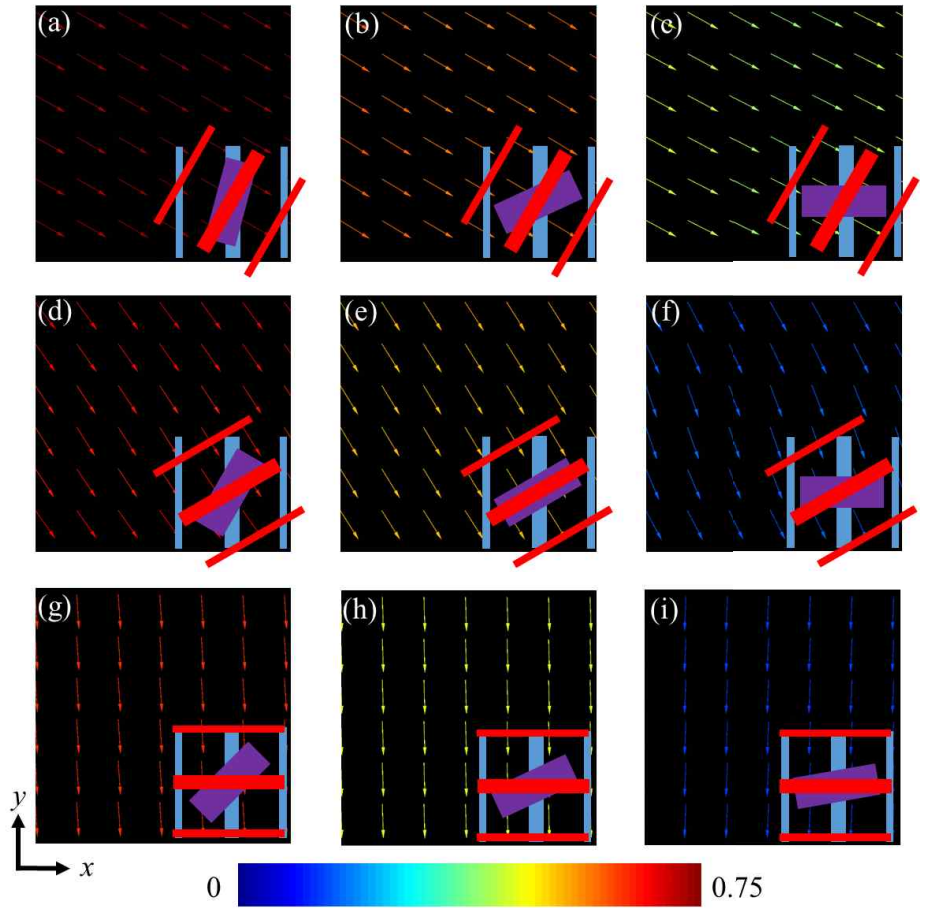

Figure 2.11 Electric field distributions of the multi-layered structures with various θ_1 and θ_2 are presented. The insets indicate the top view of the multi-layered structures with the bottom grating (blue), the nanorods (purple), and the upper grating (red). (a) θ_1 = 15°, θ_2 = 30°, (b) θ_1 = 65°, θ_2 = 30°, (c) θ_1 = 90°, θ_2 = 30°, (d) θ_1 = 30°, θ_2 = 60°, (e) θ_1 = 60°, θ_2 = 60°, (f) θ_1 = 90°, θ_2 = 60°, (g) θ_1 = 45°, θ_2 = 90°, (h) θ_1 = 65°, θ_2 = 90°, (i) θ_1 = 80°, θ_2 = 90°.

Figure 2.11 shows the calculated electric distributions at 500 nm from the surface of the upper grating layer under various θ_1 and

θ_2. The transmitted light is polarized perpendicular to the axis of the upper grating layer regardless of the twisted angle of nanorod θ_1. Also, the amplitudes change from maximum to minimum as θ_1 changes from $\theta_2/2$ to 90°. Since the light modulation is determined by the geometric parameters, it is possible to implement a spatial light modulator that can generate arbitrary transmitted amplitudes and rotation angles as shown in Fig. 2.10(a). This spatial light modulator can be realized by positioning the nanorods and the upper gratings with different θ_1 and θ_2 in each position. Figure 2.12 shows the total transmission spectra and rotation angle φ of the proposed structures with different θ_2 while changing θ_1. As can be seen, the maximum transmission occurs at $\theta_1 = \theta_2/2$, and this is a good agreement with the results of Eq. (2.5). The transmission can be tuned continuously from the maximum to minimum value by adjusting θ_1 from $\theta_2/2$ to 90° over broad wavelengths. Also, φ provides a nearly constant value and satisfies $\varphi = \theta_2$ while varying θ_1. Thus, the proposed structures can provide independent control of amplitude and polarization over broad wavelengths ranging from 700 nm to 1300 nm. The amplitude modulation depth (defined as $|E_{max}| - |E_{min}|$) reaches up to 0.9 over a broad bandwidth of 600 nm, and an arbitrary rotation angle of polarization plane can be obtained. Thus, the proposed strategy can be an excellent solution for simultaneous control of the amplitude and optical rotation without requiring any other optical components.

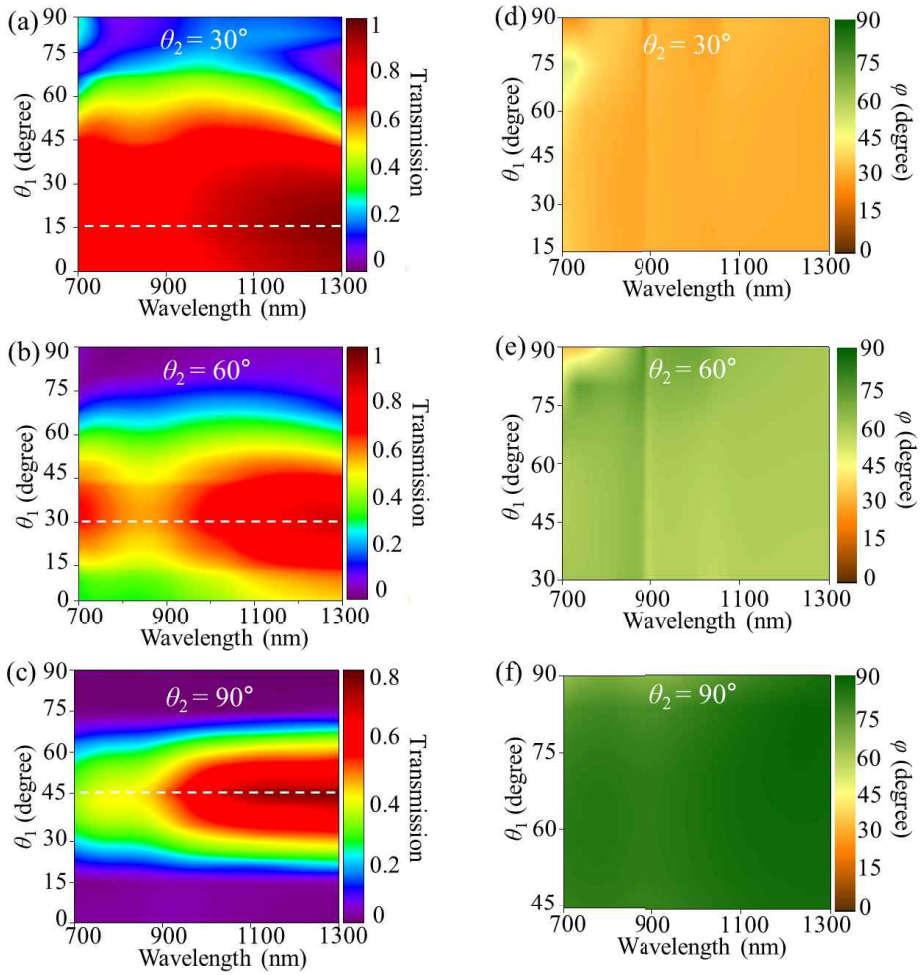

Figure 2.12 Transmission spectra obtained for the polarization–amplitude modulators with (a) θ_2 = 30°, (b) θ_2 = 60°, and (c) θ_2 = 90° while varying θ_1. The white dashed lines indicate the condition, $\theta_1 = \theta_2/2$. Rotation angle φ of the polarization–amplitude modulators with (d) θ_2 = 30°, (e) θ_2 = 60°, and (f) θ_2 = 90° while varying θ_1.

2.4 Conclusion

The proposed structures are demonstrated as a powerful solution for ultrathin polarization-amplitude modulators in transmissive optical systems. Such structures can adjust both the polarization plane of LP light and the transmitted amplitude over a wide wavelength range. Additionally, the proposed structures exhibit nondispersive optical activity originating from phase compensation among the layers and the non-resonant characteristic of the Fabry-Pérot-like cavity. Based on our structure, the simultaneous control of the polarization and amplitude is realized within a subwavelength thickness. The proposed structures provide high modulation depths for rotation by any rotation angle and amplitude of 0.9.

Here, a potential fabrication method for the proposed multi-layered metasurfaces is briefly discussed. The multi-layer structures can be manufactured by performing multiple fabrication methods using focused ion beam (FIB) [16] and electron-beam (E-beam) lithography [28]. Here, E-beam lithography is suggested as the potential fabrication method for the proposed multi-layered structure because it has advantages to fabricate large area metasurfaces. First, Al film is deposited on a glass substrate using an evaporator machine. Next, the nanopatterns are transferred to positive E-beam resist using E-beam lithography, and then the metal layer is patterned by

plasma etcher using Cl_2 BCl_3, and Ar gases [29, 30]. After fabricating the single layer, the planarization of the metasurface is conducted by spin-on glass coating. These processes can be repeated several times to produce the proposed multilayer structures. Since the proposed structures allowing only the fundamental Floquet mode are robust to interlayer alignment errors [31], the above fabrication process can be a promising method for fabricating the structures.

In addition, since the operating wavelength region is determined by plasmonic resonance of the nanorod, our design can be exploited for various wavelength regions by scaling the structures up or down. The layered metasurfaces could be fabricated by multiple lithography techniques, but with their thicknesses remaining below the operating wavelengths. Therefore, the proposed structure is a great candidate for realizing extreme miniaturization of various multifunctional nanophotonic systems. Moreover, the proposed devices can be exploited to realize functionalities such as asymmetric transmission, linear polarization conversion and amplitude modulation. For the tri-layered structure with θ = 45°, the x-polarized incident light in the forward direction (+z direction) is converted into y-polarized light with high conversion efficiency of up to 80%. In contrast, the x-polarized incident light in the backward direction (-z direction) cannot penetrate the third layer with the grating axis parallel to the x-axis. Thus, the tri-layered

structure can provide tremendous asymmetric transmission ($T_{forward}/T_{backward}$ = 10 - 170) over an ultrabroad wavelength range (550 nm - 3000 nm). Our structures offer a promising alternative to previous studies of polarization conversion and asymmetric transmission [32-34]. Therefore, it is expected that the extreme miniaturization of various optical systems can be realized based on the proposed structures.

Chapter 3. Ultracompact meta-pixels for true color generation using bi-layered hybrid metasurfaces

3.1 Introduction

Nowadays, high-end display systems are faced with the demands for compact form factors, small pixel sizes, and wide color gamut. However, such a demand has not been completely satisfied due to the difficulties of miniaturization and integration of the conventional optical elements such as color filters and polarizers. Recently, plasmonic color generations have been widely studied to generate colors at nanoscales. A wide range of color generation has been demonstrated by tuning the plasmonic resonance of the array of metallic antennas with various metals such as silver [35-38], and aluminium [39-41]. However, the plasmonic nanoantennas provide broad spectral response and low saturation colors due to intrinsic loss of the metals. Thus, to achieve highly saturated colors, dielectric metasurfaces based on the resonances in high index dielectric nanoantennas have been proposed [29, 42-46]. High refractive index dielectric materials such as silicon can support electric and magnetic resonances,

called Mie resonances [47,48], and their scattering characteristics are determined by the interferences among the resonances. Through manipulating carefully these Mie resonances, a pure color generation has been presented in reflection type dielectric metasurfaces. However, transmittance type dielectric metasurfaces suffer from low saturation colors because it is difficult to provide narrow resonance bandwidth over the entire visible wavelengths by designing the multipolar electric and dielectric resonances of dielectric structures. In addition, the aforementioned structural color generations have common limitations of low color depth (~ thousands of colors). This is because the spectral tuning relies on tiny adjustment of the length parameters such as period, radius and distances between the nanostructures. This approach makes difficult to obtain the color pixels that are expressed in the desired colors with specific hue, saturation, and value because the resonance wavelength and intensity are changed simultaneously by adjusting the length parameters [49,50]. As a result, the limited number of colors drastically degrade a resolution of a real picture and leads to limited appliactions in imaging and display systems.

Here, a novel structure of bi-layered hybrid metasurfaces is proposed to achieve highly saturated colors and high color depth generation with ultracompact form factors. The proposed bi-layered metasurfaces consisting of aluminium (Al) nanograting layers and anisotropic amorphous silicon (a-Si) nanorods can

provide independent control of spectral resonance and intensity by adjusting different geometric parameters. The hybrid metasurfaces only allow specific resonance transmittance peaks determined by size of the nanorod to be transmitted by polarization rotation originating from the rotated anisotropic nanorods. In addition, a cavity effect between the nanograting and nanorod layers permits highly saturated color generation. This is because the spectral broadening caused by the electric and magnetic multipolar resonances in the dielectric nanorods can be ameliorated by manipulating the interferences among those resonances through adjusting the distance between the layers. Also, based on the proposed structures, the method for gradual color tuning and high color depth generation is presented using additive color mixing. Spatially varying unit cell structures of the proposed hybrid metasurfaces, called meta-pixels, allow to design the spectral resonance and intensity. Through this color mixing method, myriad of color pixels having desired hue, saturation, and value can be created within subwavelength thickness, and thus it could be applied to reproduce real picture images. Therefore, the bi-layered hybrid metasurfaces can be a powerful solution for extreme miniaturization of many imaging and display systems.

3.2 Principles of the spectral modulation using the bi-layered hybrid metasurfaces

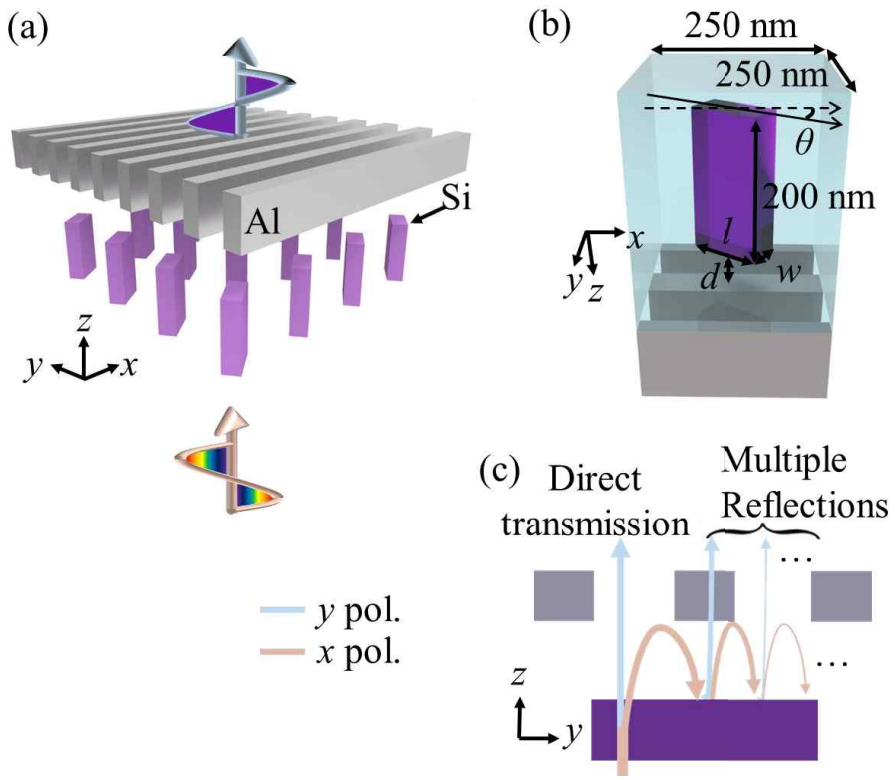

Figure 3.1 (a) Artistic rendering of the bi-layered hybrid metasurface. (b) Unit cell structure of the proposed structure. The period, thickness, and width of the nanograting are 125 nm, 40 nm, and 120 nm, respectively. (c) The unit cell structure on the *y*-*z* plane. The *x*-polarized light is incident on the rod side.

Figure 3.1 shows schematic illustrations of the bi-layered hybrid metasurfaces composed of Al nanograting layer and

rotated a-Si nanorod layer. Here, the nanograting layer is designed to act like a linear polarizer over entire visible wavelengths, and the nanorods are rotated by θ and are separated by d from the nanograting layer. When the x-polarized white light is incident on the bi-layered metasurface, the rotated nanorods rotate, depending on θ, the polarization angle of the incidence light at the resonances of the nanorods. The y-polarized component of the rotated light can pass through the nanograting layer, but the x-polarized component does not penetrate. Thus, the x-polarized component of the incident x-polarized light undergoes multiple reflections between the nanograting and nanorods until it is reflected back to $-z$ direction or converted to y-polarized light by the nanorods as shown in Fig. 3.1(c). That is, except for the y-polarized lights converted by the polarization rotations of the nanorods, the incident white light is filtered while passing through the structure.

The spectral characteristics of the rotated nanorod layer can be related to the polarizability tensor of the electric $\boldsymbol{a}$ and magnetic $\boldsymbol{b}$ multipolar resonances which are determined by dispersion of the materials and their geometric parameters [24]. When the nanorods are anisotropic and small enough compared to the wavelength of interest, electric dipole (ED) and magnetic dipole (MD) are dominantly derived and the polarizability tensors can be reduced to $\boldsymbol{a} = \begin{pmatrix} a_{xx} & 0 \\ 0 & a_{yy} \end{pmatrix}$, and $\boldsymbol{b} = \begin{pmatrix} b_{xx} & 0 \\ 0 & b_{yy} \end{pmatrix}$. For the nanorods

smaller than the wavelengths of the incident light, the nanorod layer can be modeled as the effective surface with averaged transverse polarization currents [51], and their transmission and reflection matrices can be calculated as the following equations

$$t=\begin{pmatrix} 1-\frac{i\omega}{2p_x p_y}\left(\frac{\eta_0 a_{xx}}{1-a_{xx}C_{xx}^{e}}+\frac{1}{\eta_0}\frac{b_{xx}}{1-b_{xx}C_{xx}^{m}}\right) & 0 \\ 0 & 1-\frac{i\omega}{2p_x p_y}\left(\frac{\eta_0 a_{yy}}{1-a_{yy}C_{yy}^{e}}+\frac{1}{\eta_0}\frac{b_{yy}}{1-b_{yy}C_{yy}^{m}}\right) \end{pmatrix}, \quad (3.1)$$

$$r=\begin{pmatrix} \frac{i\omega}{2p_x p_y}\left(-\frac{\eta_0 a_{xx}}{1-a_{xx}C_{xx}^{e}}+\frac{1}{\eta_0}\frac{b_{xx}}{1-b_{xx}C_{xx}^{m}}\right) & 0 \\ 0 & \frac{i\omega}{2p_x p_y}\left(-\frac{\eta_0 a_{yy}}{1-a_{yy}C_{yy}^{e}}+\frac{1}{\eta_0}\frac{b_{yy}}{1-b_{yy}C_{yy}^{m}}\right) \end{pmatrix}, \quad (3.2)$$

where p_x and p_y are periods, ω is angular frequency, η_0 is the free space impedance, C is an interaction coefficient, and the superscript e and m mean electric and magnetic, respectively. As shown in equation (3.1) and (3.2), the transmission and reflection coefficients are combination of ED and MD derived components. For convenience, the components derived from ED and MD are defined as $\alpha_i=\frac{iw}{2p_x p_y}\frac{\eta_0 a_{ii}}{1-a_{ii}C_{ii}^{e}}$ and $\beta_i=\frac{iw}{2p_x p_y}\frac{1}{\eta_0}\frac{b_{ii}}{1-b_{ii}C_{ii}^{m}}$, respectively. For the simplicity, it is assumed that the nanograting acts like a perfect linear polarizer and high order multiple reflection terms can be negligible. Similar to the method for derivation of equation (2.3), the total transmitted complex

electric field E_{tot} of the bi-layered hybrid metasurface for x-polarized incident light can be decomposed by the ED and MD components as following equations

$$\boldsymbol{E}^{e} = e^{ikn_1 d}\sin\theta\cos\theta(\alpha_y - \alpha_x)\left[1 + e^{i2kn_1 d}(1-\cos^2\theta(\alpha_x+\beta_x) - \sin^2\theta(\alpha_y+\beta_y))\right]\overline{y}, \quad (3.3)$$

$$\boldsymbol{E}^{m} = e^{ikn_1 d}\sin\theta\cos\theta(\beta_y - \beta_x)\left[1 - e^{i2kn_1 d}(1-\cos^2\theta(\alpha_x+\beta_x) - \sin^2\theta(\alpha_y+\beta_y))\right]\overline{y}, \quad (3.4)$$

$$\boldsymbol{E}_{tot} = \boldsymbol{E}^{e} + \boldsymbol{E}^{m} \quad (3.5)$$

where k is the free space wavenumber, n_1 is the refractive index of the spacer medium, and $\overline{y}$ is unit vector along with y-axis, E^e and E^m are complex electric fields caused by ED and MD resonances, respectively (see Supplementary Information for the details of the derivation). The first and second terms in the square bracket of equation (3.3) and (3.4) indicate the direct transmission and reflection components, respectively (cf. Fig. 3.1(c)). Also, it is apparent that anisotropic response of ED (α_y - α_x) and MD (β_y - β_x) resonances permit the incident light to penetrate the proposed structure as converting the incident light to y-polarized light, and the amplitude can be controlled by the rotated angle of the nanorod θ. It is also noticeable that the transmitted light is related not only to the amplitude and phase of both ED and MD resonances but also to the cavity terms governed by d. This indicate that the proposed structures give an additional degree of freedom for tuning the spectral

characteristics by adjusting d, and thus it could be fruitful to provide wide gamut of the response colors.

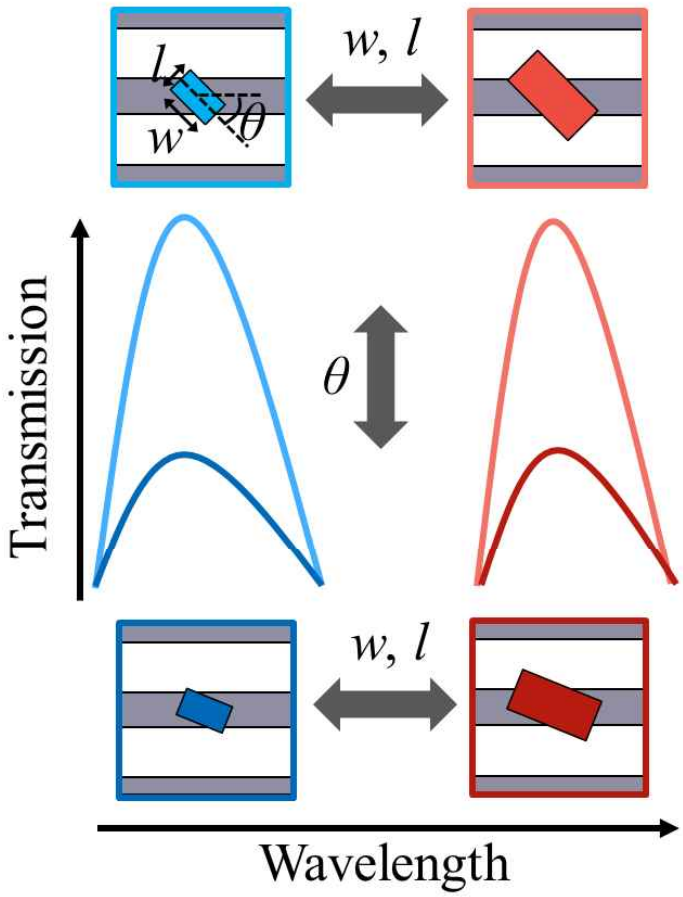

Figure 3.2 Schematic demonstration of the independent control of the spectral intensity and wavelength. The intensity and wavelength of the transmitted light can be controlled by the rotated angle (θ) and size (w, l) of the nanorods, respectively.

Based on this scenario, it is possible that the spectral resonance

and intensity are independently controlled by the different geometric parameters as shown in Fig. 3.2. The spectral resonance and intensity can be controlled by size (w, l) and θ, respectively.

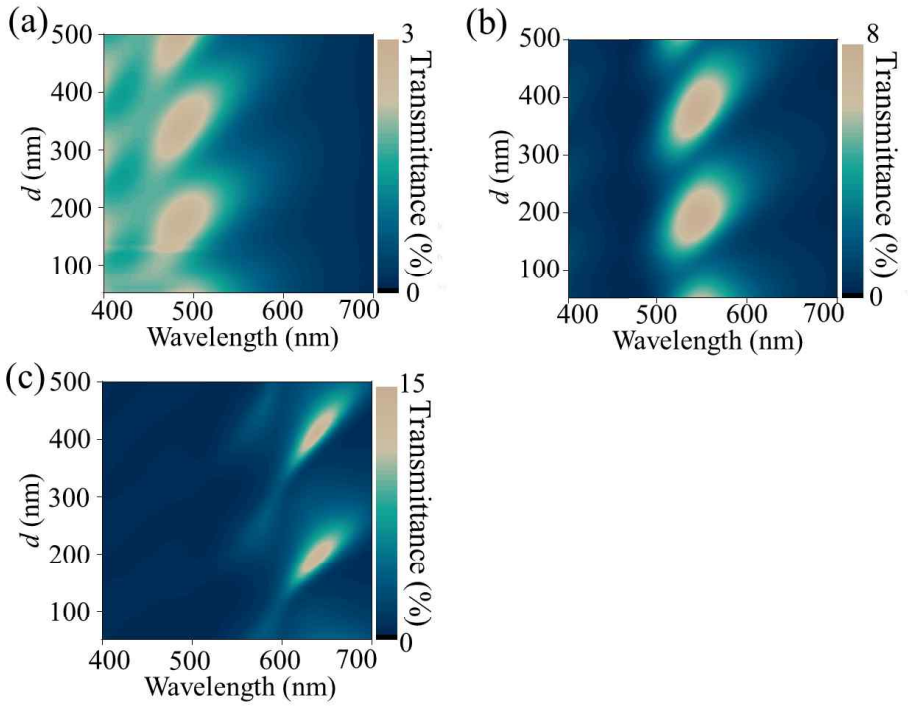

Figure 3.3 Transmittance spectra of the bi-layered hybrid metasurfaces having various nanorods of (a) w = 30 nm, l = 80 nm, (b) w = 60 nm, l = 90 nm, (c) w = 100 nm, l = 120 nm and fixed θ = 45° as changing d.

To understand the cavity effect in the bi-layered hybrid metasurface structure, the transmittance spectra of the structures having various w and l are calculated as changing d as shown in

Figs. 3.3(a)-3.3(c). Since Mie resonances are excited at longer wavelength as the sizes of nanorods increase, the spectral resonances exhibit a red shift when the size increases. As predicted in equation (3.3)-(3.5), it can be seen that the transmittances of the structures are periodically suppressed or enhanced depending on d due to the cavity effect. Moreover, it is noticeable that the resonance wavelengths and bandwidths of the structures are fluctuated as changing d.

To investigate this tendency, the spectra and electric field distributions of the bi-layered structures varying d are compared with those of the rotated nanorod layer without the nanograting. Figure 3.4(a) shows the transmittance of the y-polarized light of the nanorod layer without the nanograting (black solid line). As can be seen, the nanorod layer without the nanograting layer exhibits broad spectral response due to the electric and magnetic resonances. In contrast, the spectral bandwidth and resonance of the proposed bi-layered structures are fluctuated by d because the interferences between the Mie resonances can be adjusted through the reflection components (cf. equation (3.3) and (3.4)). In particular, the cavity effect of the bi-layered structures leads to the significant narrower full width a half maximum (HWHM) of 26 nm compared to the HWHM of the nanorod layer without the nanograting (106 nm).

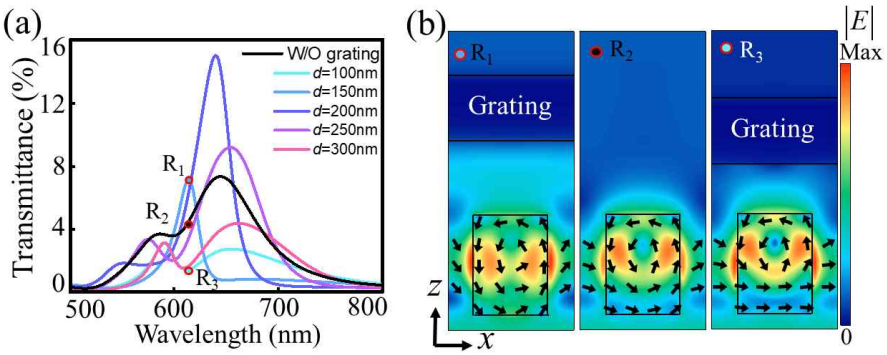

Figure 3.4 (a) The transmittance spectra of the various structures with w = 100 nm, l = 120 nm, and θ = 45°. For x-polarized incidence light, the transmitted y-polarized light of the nanorod layer without the nanograting (black line) and the transmittance of the bi-layered structures varying d (color lines) are calculated. (b) The electric distributions of various structures represented as R_1, R_2, and R_3 in Fig. 3.4(a). The R_1 and R_3 have the nanograting layer with d = 150 nm and 100 nm, respectively, and R_2 does not have the nanograting layer.

To understand the cavity effect more concretely, the electric field distributions of various structures (d = 150 nm (R_1), without the nanograting (R_2), and d = 100 nm (R_3)) at the same wavelength of 612 nm is calculated as shown in Fig. 3.4(b). For R_1, the MD resonance is dominantly excited in the nanorod, and the transmittance peak occurs at 612 nm. As the structure changes from R_1 to R_3, the ED resonance becomes stronger, and thus the transmittance decreases due to the destructive interference between the ED and MD components. This destructive interference leads to transmittance deep for R_3 through enhancing

the ED resonances and strongly supporting both of ED and MD resonances. That is, the Mie resonances in the nanorods can be controlled by the cavity effect, and the cavity effect plays a significant role in manipulations of the spectral responses including transmittance, resonance wavelength, and bandwidth. Therefore, the cavity effect can be used to make the proposed bi-layered metasurfaces to express wide color range.

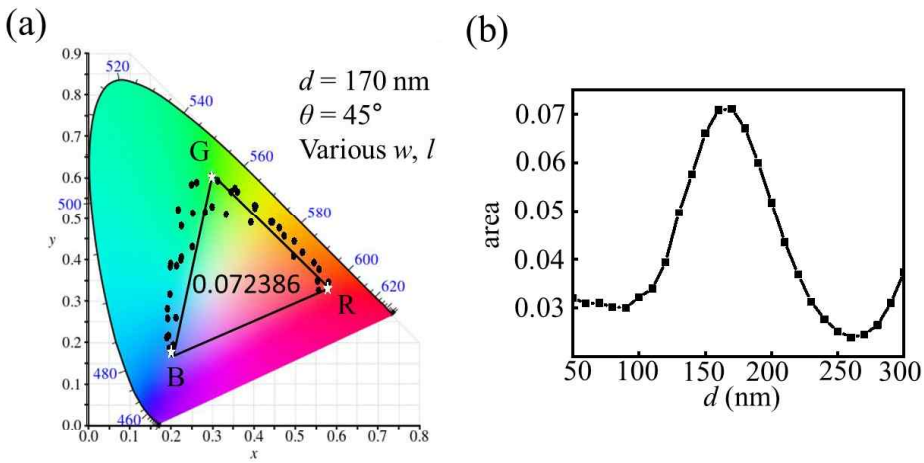

Figure 3.5 (a) Calculated CIE chromaticity diagrams of the bi-layered hybrid metasurfaces as changing w and l. The distance d and the rotated angle of the nanorods θ are set to 170 nm and 45°, respectively. The bi-layered structures with the highest purity RGB colors are indicated by white solid stars. Each RGB structure has various size of w = 30 nm, l = 50 nm (blue), w = 60 nm, l = 90 nm (green), w = 110 nm, l = 120 nm (red). (b) The area of the RGB color space of the bi-layered structures with various d.

For the color generation devices, it is important to consider not

only high transmittance but also wide color gamut which is determined by spectral bandwidth and wavelength range of the expressible colors. Figure 3.5(a) shows the CIE 1931 color space of the bi-layered structures with d = 170 nm, θ = 45°. Then, among the various nanorod sizes, the three specific structures generating RGB colors with the highest purity (highly saturated) are selected to calculate the area. Here, the area of the RGB color space is defined as the area of the triangle formed by these RGB structures. According to additive color mixing method, every points inside this RGB color space can be expressed by the combinations of the RGB colors, and thus the wider RGB color space becomes, the more the various color can be expressed. Therefore, comparing the RGB color spaces having various d could be exploited to evaluate the effect of the cavity effect in the color gamut of the proposed bi-layered metasurfaces. Figure 3.5(b) shows the calculated the area of the RGB color spaces as a function of d. As can be seen, the cavity effect leads to the fluctuation of the area ranging from 0.0239 to 0.0712. To obtain pure color and wide gamut, the optimal d is decided as 170 nm where moderate transmittance can be obtained. Moreover, to confirm the wide gamut of the bi-layered hybrid metasurfaces, the area of the RGB color space for the nanorod layer without the nanograting layer is caculated as shown in Fig. 3.6. Compared with the nanorod layer without the nanograting layer, the bi-layered structure can express more various colors at shorter

(around 480 nm) and longer (around 605 nm) wavelengths, and thus the area of RGB primary color space of the bi-layered structures can cover wider area (0.072386) than that of the nanorod layer without the grating (0.050293). As a result, the cavity effect can provide purer color, and the RGB color space of the bi-layered structure is 144% wider than that of the nanorod layer without the nanograting.

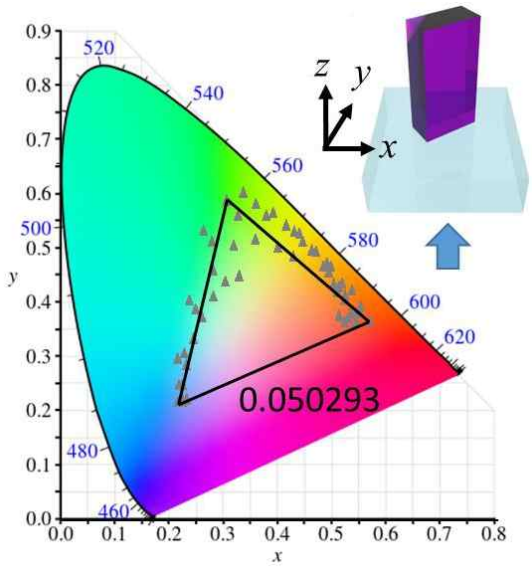

Figure 3.6 Calculated CIE chromaticity diagrams of the nanorod layers without the nanograting as changing *w* and *l*.

3.3 Independent control of the spectral resonance and intensity using the bi-layered hybrid metasurfaces

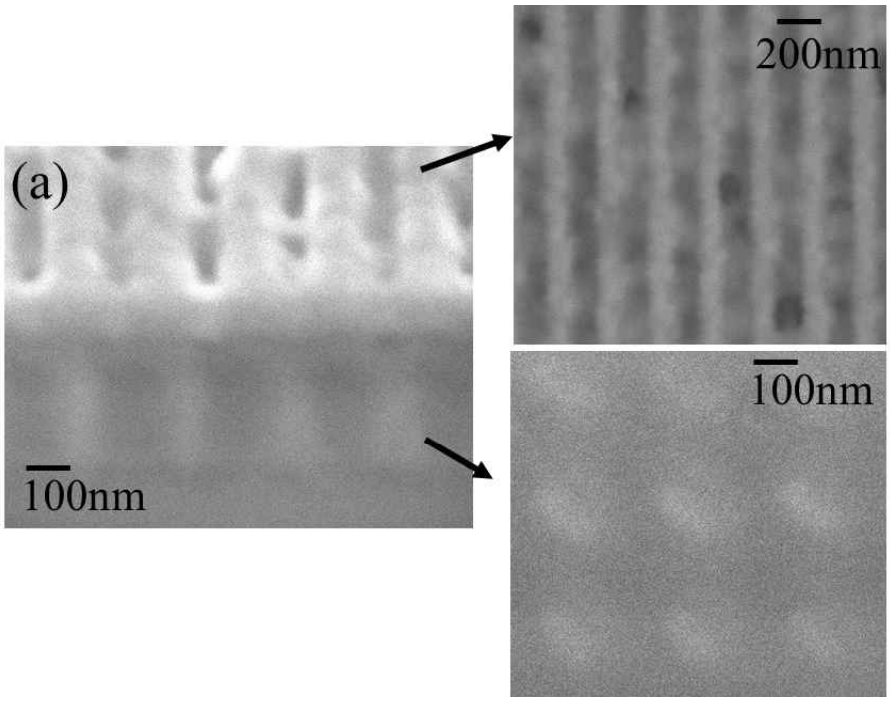

Figure 3.7 The cross-sectional (left) and the top view (right) SEM images of the fabricated bi-layered hybrid metasurface sample.

The bi-layered hybrid metasurfaces are fabricated by using conventional nano patterning techniques such as electron-beam lithography and focused ion beam milling (See following section 3.5 for details of fabrication process). Here, the nanograting layer is fabricated to have a period of 200 nm, thickness of 100 nm, and width of 100 nm in order to operate as a linear polarizer over the operating wavelengths of the input source. Figure 3.7 shows SEM

images of the fabricated bi-layered hybrid metasurfaces.

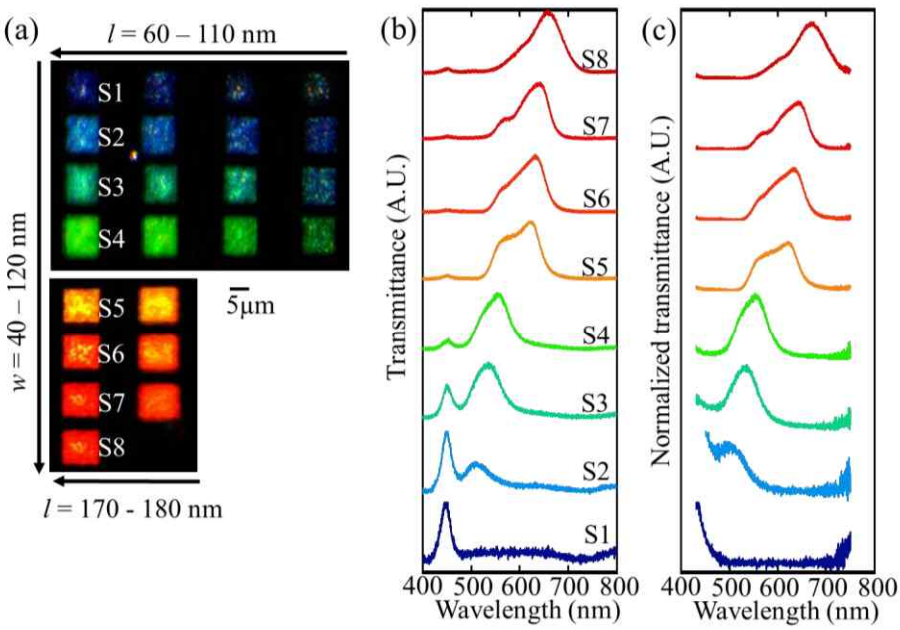

Figure 3.8 (a) Captured images of the transmitted light from the fabricated bi-layered hybrid metasurfaces with θ = 45° and various w and l. (b) Transmittance spectra of the fabricated samples (S1 – S8) and (c) the spectra normalized by the intensity of the source LED.

The fabricated samples have various size of nanorods and θ = 45°, and their transmitted lights for normal incidence of x-polarized white LED light are captured by a camera as shown in Fig. 3.8(a). As can be seen, the response colors of the fabricated structures exhibit a red shift as the sizes increase and express from blue to red. Also, it is can be seen that the intensity of the transmitted light increases as l increases. This tendency is because the

transmitted intensity of the proposed structure is proportional to the anisotropy of the nanorods as demonstrated in equation (3.3) and (3.4). Figure 3.8(b) shows the transmittance spectra of the fabricated samples with various size of the nanorods. The resonance wavelengths of the samples are gradually shifted from 450 nm to 660 nm when the size increases. The transmittance deeps occurring around 480 nm originate from the transmittance deep of the input source. Also, it can be understood that the cavity effect successfully inhibits the spectral broadening from the Mie resonances in that the spectral responses maintain narrow bandwidth over the various visible wavelengths. Moreover, as can be seen in Fig. 3.8(c), the proposed structure can control the transmitted light varying blue to red regardless of the input source spectrum. To compare the experimental results and simulations, CIE1931 color space of the spectral responses of the bi-layered hybrid metasurfaces is presented in Fig. 3.9. At the short wavelength range, the response colors undergo a slightly low saturation due to imperfection of the fabricated nanograting layer which permits transmittance of the undesired *x*-polarized light. However, the pure colors can be generated at the long wavelength range, and the response colors of the fabricated samples can cover as wide area as the color space of the simulation result.

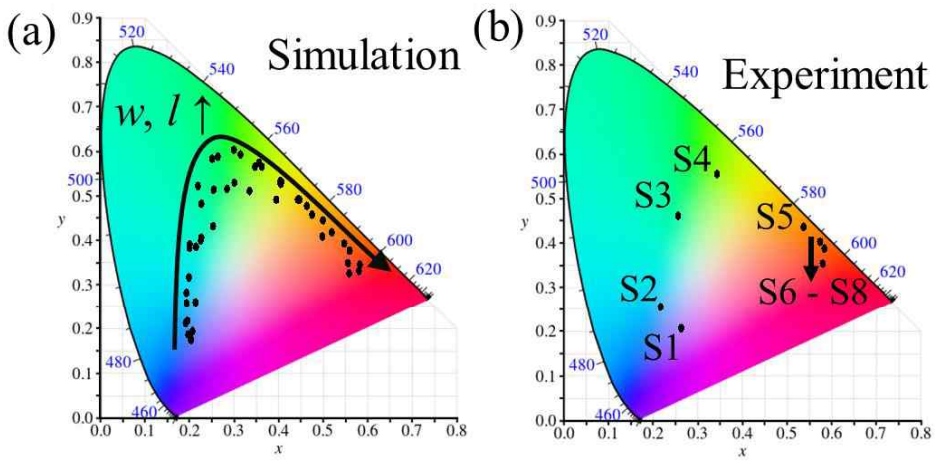

Figure 3.9 CIE chromaticity diagrams of the simulation (a) and experimental results (b). The simulation results are calculated for the proposed structures with various size (w = 30 ~ 110 nm and l = w + 10 ~ 120 nm) at θ = 45° and d = 170 nm.

Next, to independently control the intensity of the response color, the bi-layered hybrid metasurfaces with varying θ while keeping the size of the nanorods are fabricated. Figure 3.10 shows the images and spectra of transmitted colors from the fabricated samples that generate RGB colors. As can be seen in the captured images, the intensities of the RGB samples decrease, retaining their hue and saturation, and finally the response colors become black while θ changes from 45° to 0°. This intensity control can be clearly shown in the spectra as shown in Figs. 3.10(d)-(f). The resonance wavelengths of each RGB sample keep nearly constant regardless of θ, and the intensities decrease as θ decreases. Also, it can be observed that the spectral distortions are exacerbated at θ = 0°

due to the imperfection of the nanograting layer leaking the unwanted *x*-polarized light. This distortion can be addressed by fabricating the homogeneous nanograting layer operating as a perfect linear polarizer. Nevertheless, it is shown that the independent control of spectral resonance and intensity can be obtained by adjusting the size and rotated angle of the dielectric nanorods, respectively.

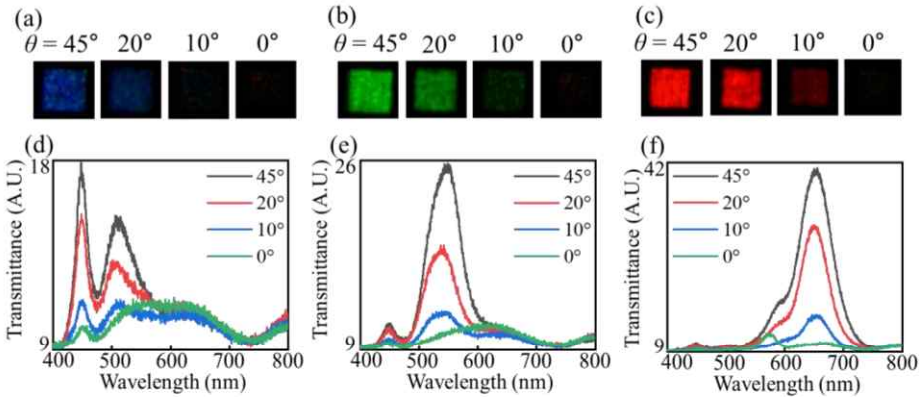

Figure 3.10 Captured images of the transmitted lights from the fabricated bi-layered structures with varying θ while keeping (a) w = 45 nm, l = 90, (b) w = 60, l = 100, (c) w = 120, l = 180. Transmittance spectra of the fabricated samples with (d) w = 45 nm, l = 90, (e) w = 60, l = 100, (f) w = 120, l = 180.

3.4 Meta-pixels for high color depth generation

3.4.1 Concept of the meta-pixels based on additive color mixing method

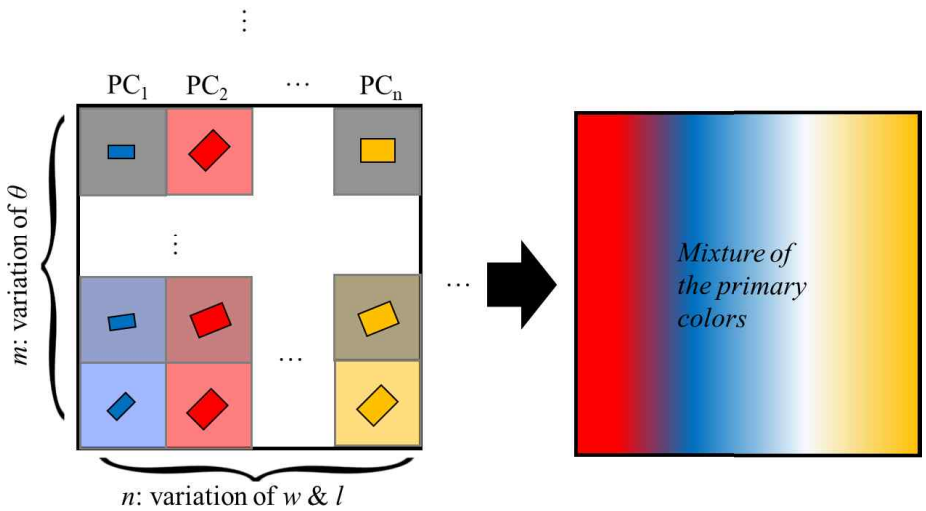

Figure 3.11 Schematic illustration of supercell structure of the proposed meta-pixel. For simplicity, the nanogorating layer is omitted in this illustration.

Intuitively, the aforementioned bi-layered metasurface can provide high resolution color pixels that are achieved by placing the nanorods having various size (w and l) and θ at different positions. However, gradual tuning of hue, saturation, and value of the response color is still challenging due to limited tunability of the length parameters (w and l). To overcome this low color depth, meta-pixels which can provide gradual tuning of colors

based on additive color mixing is proposed. Figure 3.11 demonstrates $n \times m$ meta-pixel that is supercell structure of the proposed bi-layered metasurfaces having various w, l and θ. Each sub-pixel of the meta-pixel changes the size of the nanorods (w & l) along the columns and changes θ along the rows. In other words, each column represents different n primary colors, and the total intensity of each primary color is encoded by the sum of their θ. According to additive color mixing method, the meta-pixels can express various colors inside the color space composed of the primary colors of the sub-pixels, and the response chromaticity (hue and saturation) can be controlled by adjusting the ratio of the primary colors. Also, the value of the meta-pixel can be controlled by adjusting θ while keeping the ratio of the primary colors. Thus, the expressible number of colors of the meta-pixel (#C) can be decided by following equation

$$\#C = \left(\frac{45^\circ}{\Delta\theta} m \right)^n \tag{6}$$

where $\Delta\theta$ indicate the variation of the rotated angle of the nanorods θ. The gradation of each primary color is assigned by $\frac{45^\circ}{\Delta\theta} m$. Thus, gradation of the finally created colors becomes smoother and continuous as $\Delta\theta$ and m become smaller and larger, respectively. Also, increasing the number of primary colors (n) is very profitable in that #C increases exponentially, and it allows to cover wide area in the color space.

3.4.2 Gradual tuning of the response colors using the meta-pixels

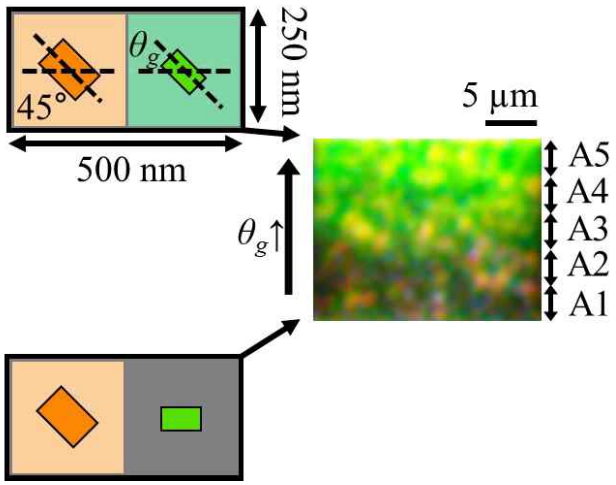

Figure 3.12 Schematic illustration of the supercell structures of the 1 × 2 meta-pixel with orange and green sub-pixels (left), and the image of the transmitted light from the fabricated meta-pixel sample (right). The rotated angle of the orange sub-pixel is fixed at 45°, and the rotated angle of the green sub-pixel (θ_g) changes from 0° to 45°.

As an example, the 1 × 2 meta-pixel that has orange and green as primary colors is demonstrated as shown in Fig. 3.12. The rotated angle of the green pixels (θ_g) changes from 0° to 45° while that of orange keeps 45°. As shown in the captured image of the transmitted light of the fabricated meta-pixel sample, it can be observed, in spite of high magnification of the image, that the response color changes from orange to yellow and then from yellow to green as θ_g increases. To understand this gradual color changes more clearly, the fabricated

sample is divided into five regions (A1 – A5), and the transmittance spectra and CIE color space of each region are investigated as shown in Fig. 5.13.

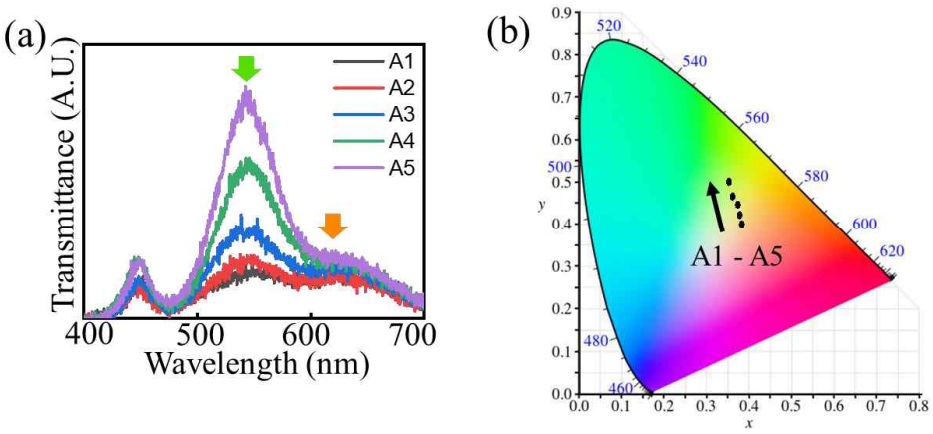

Figure 3.13 Experimentally measured (a) Transmittance spectra and (d) color space of the meta-pixel sample divided by five areas (A1 – A5).

The resonance wavelengths of the orange and green pixels can be found at 618 nm and 542 nm, respectively. Also, it can be seen that the intensity of the resonance at 542 nm can be independently controlled by θ_g while that of the resonance at 618 nm remains nearly constant. As a result of this spectral changes, the response colors of the meta-pixels can gradually change on the straight line connecting the two primary colors (orange and green) in the color space as shown in Fig. 5.13(b). Compared with the method for controlling the chromaticity by adjusting the size of nanorods (cf. Fig. 3.9), the proposed meta-pixels based on additive color mixing can be used to more gradually tune the

response colors, and the gradation can be improved by increasing $\Delta\theta$ and m. In addition, as can be seen in Fig. 5.13, the response color of the meta-pixels can be intuitively predicted according to the additive color mixing method. Therefore, it is a promising solution for generating high color depth and reproducing real pictures to exploit the proposed meta-pixels.

3.5 Fabrication and optical measurement

In this section, the details of the fabrication process and optical measurement for the proposed bi-layered hybrid metasurfaces are demonstrated.

3.5.1 Fabrication process

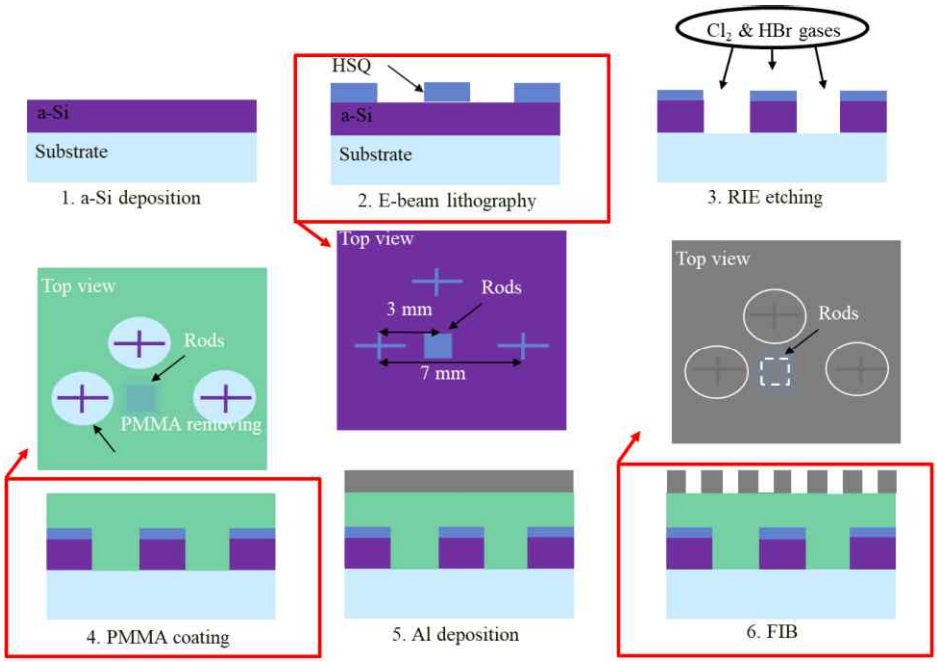

Figure 3.14 Fabrication flow chart for the bi-layered hybrid metasurfaces.

For fabrication of the bi-layered hybrid metasurfaces, conventional nano-fabrication techniques such as focused ion beam (FIB) milling and electron beam lithography methods are

used. Figure 3.14 shows the flow chart of the fabrication process for the bi-layered hybrid metasurfaces. Firstly, silicon oxide of 100 nm and a-Si thin film of 200 nm is sequentially deposited on quartz wafer substrate using PECVD (AMAT P5000, OEM group). The refractive index of the deposited a-Si film is measured by ellipsometer (J. A. Woollam, V-VASE). Next, a negative-tone resist (XR-1541-006, Dow Corning) is spin-coated, and then the nanorod patterns are transferred to the resist using electron beam lithography (JBX-6300FS, JEOL) and developed. For the multi-layered metasurfaces, it is important to align the sequentially stacked multiple layers. Therefore, the cross-line-shaped reference marking structures are also transferred to the resist as shown in Fig. 3.14. The patterns are transferred to the a-Si layer via inductively coupled plasma etching with Cl_2 and HBr gases. For the planarization, PMMA (950PMMA A4, Micro Chem) is spin-coated on the sample, and then the PMMA coated on the reference markings are cleaned up by acetone solution before the bake process. Next, the 100-nm-thickness of Al is deposited using an E-gun evaporator (ZZS550-2/D, Maestech). Finally, the nanograting patterns with period of 200 nm are milled at the Al layer by FIB milling machine (Quanta 200 3D, FEI). At this time, the position of the nanorods layer should be aligned with the grating layer. The align process is explained in Fig. 3.15. Because the PMMA removal hinders the planarization on the reference marking structures, they can be observable after the Al

deposition.

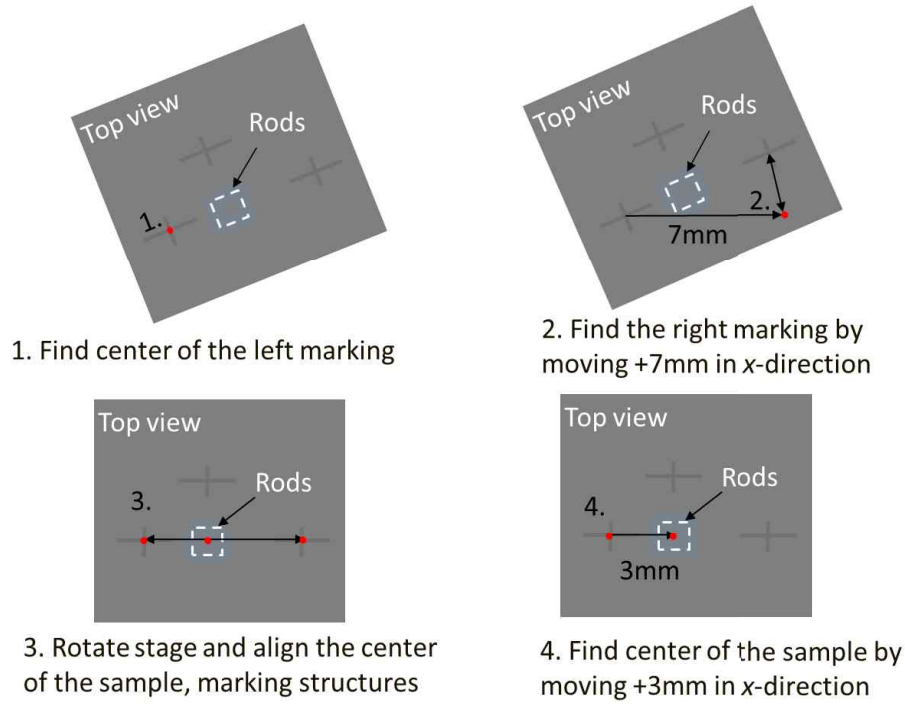

Figure 3.15 Flow chart for aligning the multi-layered structures.

The relative position of the marking structures indicates the $+y$ direction of the nanorod patterns. Firstly, find the center position of the left marking structure. And then, parallel moving the FIB sample stage in parallel to $+x$ direction to find the right marking structure. This process instructs the rotated angle of the stage. Next, rotate the sample stage to align the center positions of the left and right marking structures on the straight line parallel to x-axis of the sample stage. After this process, the nanorods can

easily found by translational shift of the sample stage.

3.5.2 Optical measurement

The fabricated bi-layered hybrid metasurfaces is illuminated from the substrate side using a broadband white light LED (MNWHL4 LED, Thorlabs). The spectrum of the LED source is experimentally measured as shown in Fig. 3.16. the spectrum of the LED source exhibits broad wavelengths. Also, it is seen that the transmittance deep is observed at 480 nm due to the narrow bandwidth of the blue light composed of the white LED. This transmission deep results in the transmittance deep of the fabricated color pixel samples in Fig. 3.8(b).

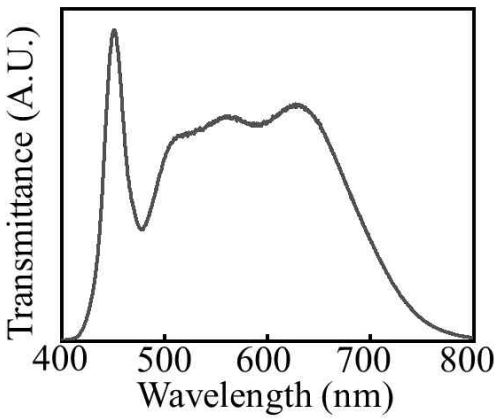

Figure 3.16 The experimentally measured spectrum of the input LED source.

The LED source is illuminated through a broadband linear

polarizer (High Contrast Glass Linear Polarizers, Edmund Optics) aligned perpendicular to the nanograting axis and 10X or 50X objective lens. The lights transmitted through the samples passes a linear polarizer aligned parallel to the nanograting axis, and then their microscopic images are captured by camera (UCMOS05100KPA, Touptek), and the spectra are measured by spectrometer (Princeton Instruments, SpectraPro 2300).

Actually, the additional linear polarizer parallel to the grating is not needed if the grating layer perfectly prohibits the undesired *x*-polarized light. However, the undesired x-polarized light is transmitted through the fabricated grating layer due to the imperfection of the grating layer. This leads to the degradation of purity of the response colors of the proposed structures as shown in Fig. 3. 17(a). The captured images from the color pixels with various *w*, *l* (same as Fig. 3.8(a)) are taken without the polarizer parallel to the grating axis. Compared with the experimental results with the polarizer (cf. Fig. 3.8(a)), it is clearly seen that the unwanted *x*-polarized light leaked from the grating layer leads to low saturation of response colors. Moreover, it is not sufficient to reject the x-polarized light that using an additional polarizer. Figures 3.17(c) and 3.17(c) show the transmittance spectra and the captured images (with the additional polarizer) of the blue color pixel and the fabricated single grating layer. As can be seen, the unwanted x-polarized light is slightly transmitted through the structure and the polarizer. Therefore, it

is significantly important that the high quality grating layer that can perfectly prohibit the undesired *x*-polarized light.

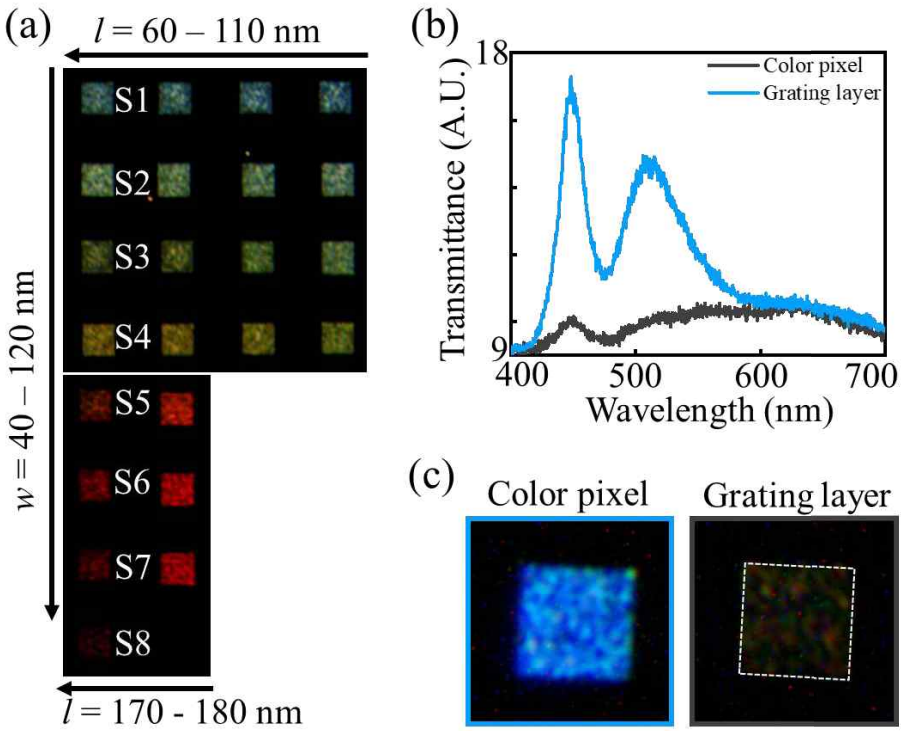

Figure 3.17 (a) Captured images of the transmitted light from the fabricated bi-layered hybrid metasurfaces with θ = 45° and various w and l, without the polarizer parallel to the grating axis. (b) Transmittance spectra of the blue color pixel (blue line) and single grating layer (black line) with an additional polarizer. (c) The captured images of the transmitted light from the color pixel (left) and the single grating layer (right) with an additional polarizer.

3.6 Discussion & Conclusion

3.6.1 Reflection type structures

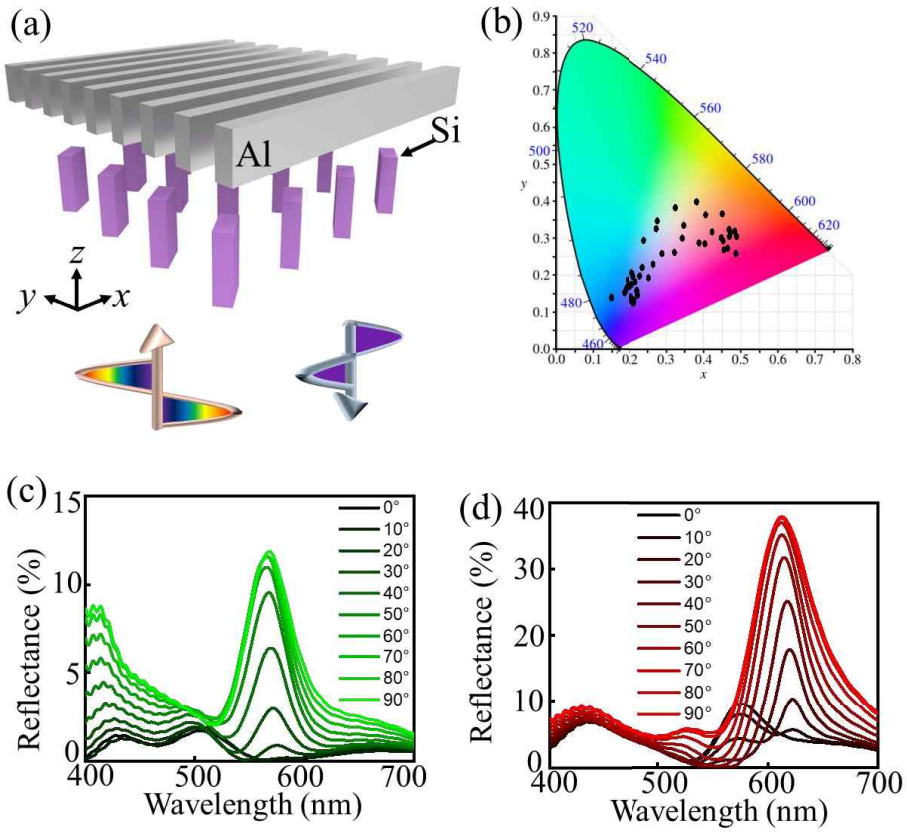

Figure 3.18 (a) Schematic illustrations of the reflection type color pixel structures. (b) CIE diagrams of reflected *y*-polarized lights of the reflection type structures varying sizes (*w*, *l*) of the nanorods. The reflection spectra of *x*-polarized light from the structures with (c) *w* = 50 nm, *l* = 110 nm, (d) *w* = 80 nm, *l* = 120 nm as changing the rotated angle of the nanorods.

Intuitively, the underlying physical mechanisms of the bi-layered hybrid metasurfaces can also be applied to the reflection type color pixels as shown in Fig. 3.18(a). When *y*-polarized light is incident on the reflection type structures, *x*-polarized light converted, through the cavity effect and the optical rotation of the nanorods, is reflected back. Figure 3.18(b) shows the CIE color space of the reflected x-polarized lights from the reflection type structures having various *w*, *l*. It can be seen that the structure can express various colors ranging from blue to red but they exhibit low saturation. The reason for the low luminance is that strong reflections of high order Mie resonances occur in the short wavelength region. This unwanted spectral broadening can be seen in Figs. 3.18(c) and 3.18(d). The reflectance efficiency exhibits relatively high however the higher order resonances excited in short wavelengths are not sufficiently attenuated according to the rotated angle of the nanorods.

3.6.2 Conclusion

The independent control of spectral resonance wavelength and intensity with narrow bandwidth is demonstrated in the proposed bi-layered hybrid metasurfaces. Also, a potential method for generating high color depth is presented by the proposed meta-pixels. The proposed structures have been successfully demonstrated by theoretical and experimental analysis, but some

improvements are needed to apply them to practical imaging systems.

Firstly, the fabrication method for the homogeneous nanograting layer in large area is required. Actually, it is hard to fabricate the nanograting of a period of several hundred nanometers over a wide area by using FIB milling technique. Therefore, nanoimprint lithography, which has been reported to successfully fabricate high quality visible polarizers in centimeter scales, could be a promising solution for fabrication of the nanograting layer. Secondly, a potential of the bi-layered structures as dynamic color pixels will be addressed. To achieve dynamic color pixels, it would be a possible solution to replace the a-Si nanorods with phase change materials [52-54] that changes their refractive index according to the external stimuli. The size of the phase change material nanorods would decide the resonance wavelength, and the refractive index variation would result in the transmittance changes by manipulating the anisotropy of the rotated nanorods.

The bi-layered hybrid metasurfaces have significant advantages in ultrathin thickness and high color depth generation. Therefore, it is expected that the bi-layered structure can be a promising candidate for the next generation imaging systems such as flexible and foldable displays.

Chapter 4. Broadband ultrathin circular polarizer using helically stacked nanogratings

4.1 Introduction

A circular polarizer has played significant roles in optics. With the increasing importance of polarization resolved imaging system, circular polarizers have been applied to enhanced contrast [55], circular polarization microscopy [56,57], remote sensing of chiral signatures [58], and detection of biomolecules such as amino acid, DNA and glucose which have inherent chiral structures [56, 58-60]. Especially, circular polarizers operating at visible wavelength have attracted much attention because they are exploited as crucial optical components to control the polarization state of light in the complex display systems such as three-dimensional (3D) displays for virtual reality and augmented reality (VR/AR) [61]. Conventionally, a circular polarizer is achieved by a combination of several polarizers. However, this polarization system has limitation in various applications due to bulky configuration and narrow operating bandwidths.

Recently, metamaterials with 3D helix structures have been

demonstrated as potential solutions for broadband circular polarizers because of their thin thickness and broad bandwidth. The 3D helix metamaterials can be fabricated by using various fabrication processes such as direct laser writing (DLW) [5, 62], DNA based self-assembly [63], focused ion beam induced deposition (FIBID) [64], focused electron beam induced deposition (FEBID) [65], glancing–angle deposition (GLAD) [66, 67], and tomographic rotatory growth (TRG) [68]. With the 3D helix structures, broad bandwidth and high circular polarization selectivity are achieved at infrared frequencies. However, the aforementioned fabrication techniques are incompatible with the other optical components, and thus they have limitation in fabricating the circular polarizer integrated nanophotonics systems.

As an alternative approach, stacking a few layers of planar metasurfaces within the subwavelength distance has been proposed [69-75]. As twisting and stacking multiple metasurfaces layers, strong resonance in a single layer of metal inclusions is converted into broadband bianisotropic effect by magneto-electric coupling among the stacked layers. This approach is more attractive solution than the aforementioned 3D helix structures because it can be fabricated by the multiple conventional lithography techniques such as focused ion beam and electron beam lithography. The stacked metasurface based circular polarizers have been implemented in various wavelength ranges

of microwave [69,70], infrared [72,74], and near-infrared [6,73]. However, on these resonances based structures, the trade-off between bandwidth and resonance strength is inevitably accompanied, and thus it is hard to achieve high circular polarization selectivity and broad bandwidth simultaneously. Also, it is difficult to realize visible circular polarizer made of gold or silver inclusions because these noble metals have low plasma frequencies [76,77]. Therefore, broadband circular polarizers operating in the entire visible wavelength range have remained as a key challenge. In addition, precise alignment between the stacked unit cell structures is required, that increases complexity in the fabrication process. As a result of these limitations, the helically stacked metasurfaces with noble metals are far away from application to the practical polarizer integrated imaging systems even though they have great advantages in ultra-thin thickness and broad bandwidth.

In this section, an ultrathin circular polarizer operating over entire visible wavelengths is proposed. The proposed structure having helically stacked multiple nanograting layers which lead to non-resonant chiral current loop. By exploiting non-resonant and broadband anisotropic characteristics in the nano-gratings, the proposed structure provides distinct 3D chiral current loops depending on the polarization state of light. This gives a detour route for avoiding the trade-off relation between circular polarization selectivity and bandwidth, so that it is possible to

achieve both properties simultaneously. Thus, it can be indicated that the proposed structures are different from the double-layered gold crossed-gratings with symmetry breaking structures and resonant characteristics in ref. 24. Also, fabrication process is simplified by alignment-free multiple lithographies as the proposed design is based on twists of whole nano-grating layers rather than twists of unit cell structures. The induced current distributions impinged by the circularly polarized (CP) light are investigated to demonstrate circular polarization selectivity in the proposed design. Finally, in order to investigate the fabrication feasibility and circular polarization selectivity of the proposed structure, experimental demonstration is presented by fabricating a prototype of the proposed structure using successive ion-beam millings and multi-wavelength optical measurements.

4.2 Circular polarizer using helically stacked nanogratings

4.2.1 Basic principle

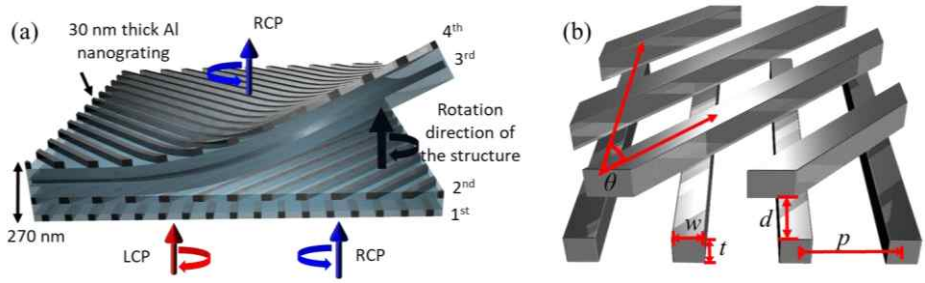

Figure 4.1 (a) Schematic illustrations of the proposed helically stacked Al nano-grating structure for visible wavelength ranges. (b) The magnified schematic of the double-layered Al nano-grating structure. The nano-gratings have period (p), width (w) and thickness (t), and they are helically stacked with twisted angle (θ) and separation (d).

The proposed broadband circular polarizer that is hellically stacked aluminum (Al) nano-gratings as shown in Fig. 4.1. Specifically, each layer consists of Al nano-gratings, and they are stacked in gradually twisted manner with subwavelength separation d and twisted angle θ. For the clockwise stacked proposed structure, left circularly polarized (LCP) incident light rotating in the same direction as the structure forms 3D chiral current loop and is reflected back. In contrast, right circularly polarized (RCP) light weakly interacts with the structures, and

thus feels that the structures are almost transparent.

4.2.2 Non-resonant characteristic of helically stacked nanogratings

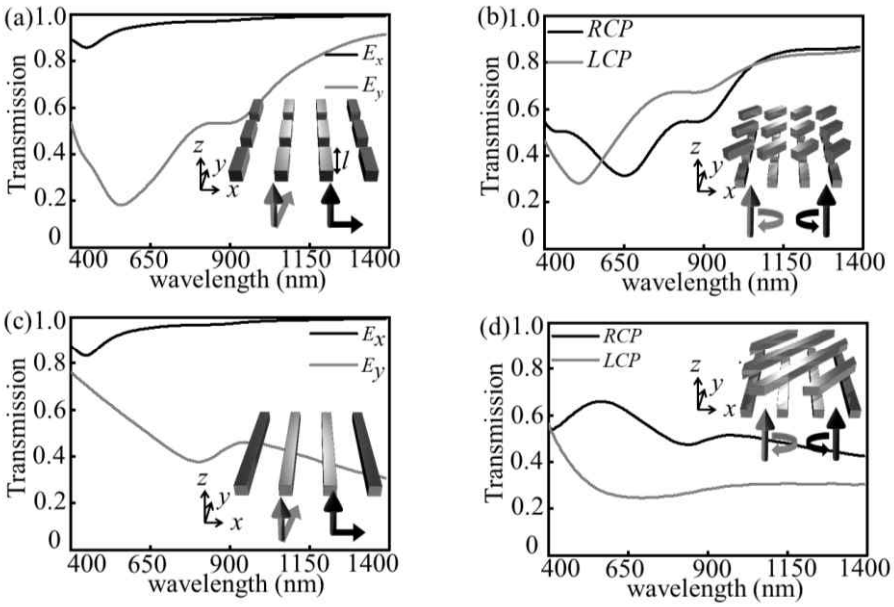

Figure 4.2 (a) Transmission of Al nanorod array for the LP light and (b) helically stacked nanorod array for the CP lights. The nanorods have p = 150 nm, l = 100 nm, w = t = 30 nm. The bottom nanorods are parralel to y-axis, and the upper nanorods are helically stacked with d = 50 nm and θ = 45°. (c) Transmission of Al nano-gratings for the LP light and (d) helically stacked nano-gratings for the CP lights (d) with p = 150 nm, w = t = 30 nm, d = 50 nm and θ = 45°.

For comparison, transmission properties of nanorod and nano-grating based structures are examined first by numerical analysis. In this section, all numerical simulations are performed by

commercial finite-difference time-domain tool (FDTD, Lumerical Solutions, Inc.). Dielectric constants of Al are referred to the textbook [26] and the refractive indexes of substrate and dielectric spacer between stacked layers are assumed as 1.5. For calculation of transmission matrices for CP light, the simulations are conducted under the LP incident light (*x* and *y* polarized incident light). Hence, the following equation is used:

$$T_{cir} = \begin{pmatrix} T_{rr} & T_{rl} \\ T_{lr} & T_{ll} \end{pmatrix} = \frac{1}{2}\begin{pmatrix} \left(T_{xx}+T_{yy}\right)+i\left(T_{xy}-T_{yx}\right) & \left(T_{xx}-T_{yy}\right)-i\left(T_{xy}+T_{yx}\right) \\ \left(T_{xx}-T_{yy}\right)+i\left(T_{xy}+T_{yx}\right) & \left(T_{xx}+T_{yy}\right)-i\left(T_{xy}-T_{yx}\right) \end{pmatrix} \quad (4.1)$$

where the subscripts *r* and *l* represent the right circularly RCP and LCP light, respectively.

The calculated transmission spectra of the Al nanorods for LP light and the double-layered one for CP light are shown in Figs. 4.2(a) and 4.2(b). The Al nanorods with anisotropic structure make plasmonic resonances at different wavelengths depending on the polarization state of incident light. As shown in Fig. 4.2(a), the Al nanorods, for *y*-polarized light which is parallel to the nanorod axis, exhibit the strong resonant transmission dip at the wavelength of 558 nm. Also, the weak transmission dip occurs around 880 nm due to the intrinsic optical loss of Al. On the other hand, for *x*-polarized light which is vertical to the nanorod axis, the incident light easily passes through the nanorods without strong resonance over the wavelength range.

Also, it is worth noticing that the anisotropic transmission in the entire visible range is obtained, which is difficult for gold and silver nanostructures since Al provides plasmonic resonance at shorter wavelength than that of the noble metals. When the unit cell of the nanorod array is twisted and closely stacked within subwavelength distance of d = 50 nm and twisted angle θ = 45° (inset of Fig. 4.2(b)), the LP eigenmodes on each single nanorod can be converted into CP ones by magneto-electric coupling between the cascaded nanorod layers. As shown in Fig. 4.2(b), the helically stacked two-layered nanorods show resonant transmission dips at 508 nm and 653 nm for LCP and RCP incident light, respectively. These distinct transmission dips depending on the polarization state of incident light lead to moderate circular polarization selectivity: RCP light selectively passes through the structure between 320 nm and 575 nm, while LCP light mainly passes through it between 575 nm and 780 nm. However, since this bianisotropic effect is based on the strong resonance in the nanorods, high *ER* and broad bandwidth cannot be achieved simultaneously by this resonance based structure. Next, non-resonant metamaterial is considered, which provides low optical loss and broad bandwidth [78,79]. Al nano-gratings are exploited as shown in Fig. 4.2(c). The nano-gratings allow current to flow in a nearly infinite length on y-axis, but not on x-axis. Therefore, the nano-gratings exhibit non-resonant characteristics over the wide wavelength range of y-polarized

light, but do not interact much with the *x*-polarized light. As shown in Fig. 4.2(c), the Al nano-grating layer transmits *x*-polarized light and reflects *y*-polarized light over broad wavelength range with a small transmission dip around 800 nm due to intrinsic loss of Al. It is easy to confirm that the nano-grating layer results in non-resonant and broadband anisotropic transmission from visible to telecommunication wavelength ranges. Then, the nano-gratings are stacked helically with twist of the entire nano-grating layer, rather than twisting the unit cell structure (Fig. 4.2(d)). As shown in Fig. 4.2(d), it is apparently shown that the stacked nano-gratings, over the extremely broad wavelengths ranging from visible to telecommunication wavelengths, selectively transmit RCP light quite well, but the most of LCP incident light is reflected.

Extinction ratio (*ER*) and figure of merit (*FOM*) of the helically stacked nano-gratings and nanorods are compared over operating bandwidth as shown in Fig. 4.3. Here, the operating bandwidth is defined as a wavelength span where *ER* is larger than $\sqrt{2}$, and *FOM* is defined by a product of the operating bandwidth and the averaged *ER*. The proposed nano-grating structure can provide the operating bandwidth of 922 nm and the *FOM* of 1816, which are about 8 times larger than those of the helically stacked nanorod structure.

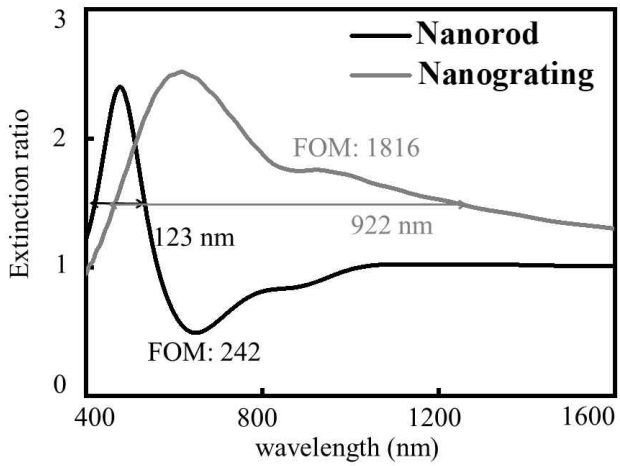

Figure 4.3 Extinction ratio (T_{RCP}/T_{LCP}) and operting bandwidth of the stacked nanorod (black) and nano-grating (gray).

To understand the underlying mechanism of the stacked nano-grating structure, electric current density in the stacked nanorod and the stacked nano-grating structures are compared as shown in Fig. 4.4. In this section, the effective material parameters are not exploited because the proposed multiple layered structure comes from complicate interaction among the nano-grating layers. When the nanorod array is excited by the light polarized along the nanorod axis, free electrons are accumulated on both ends of the nanorod, and strong oscillation of current flows through the nanorod. In the case of the helically stacked nanorods, the strong oscillation of current in the bottom nanorods is transferred to the next upper nanorod by the magneto-electric coupling between the nanorods.

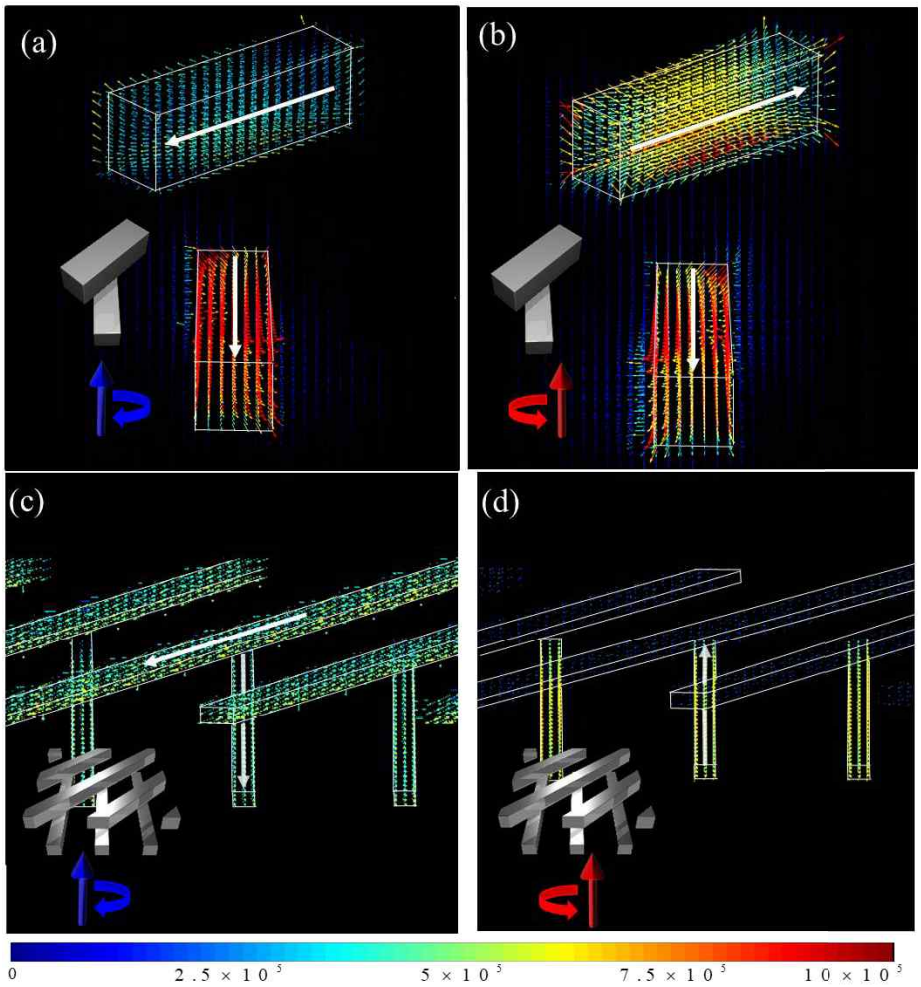

Figure 4.4 Electric current distribution in the helically stacked Al nanorods (a) for LCP incident light at 508 nm and (b) RCP incident light at 653 nm. Electric current distribution in the helically stacked Al nano-grating for (c) LCP and (d) RCP incident light at 609 nm. The white arrows indicate the direction of the induced current.

Hence, 3D chiral current loop is formed. For LCP incident light, the helically stacked nanorods with left handed manner cause the

resonantly induced currents to flow in the same direction in the bottom and the upper nanorods (anti-bonding mode) at the resonance of 508 nm (Fig. 4.4(a)). For RCP incident light on the left handed configuration, similar resonant transmission dip occurs but it resonates at the longer wavelength of 652 nm (Fig. 4.4(b)), because the currents form the bonding mode. On the other hand, in the case of the nano-gratings, when the LP light parallel to the nano-grating is incident on the structure, the induced current path becomes infinitely long. When the nano-gratings are helically stacked, the stacked structure forms quite different current distribution depending on the handedness of the incident light. For LCP incident light, the stacked nano-gratings with left handed manner induced current flows to the upper layer and exhibit relatively strong magneto-electric coupling. This coupling leads to 3D chiral current flows and provides high reflectance (Fig. 4.4(c)). On the other hand, for RCP light, the induced current at the bottom layer cannot strongly interact with the upper layer (Fig. 4.4(d)). Therefore, the proposed structure exhibits weak 3D chiral current loop and acts like nearly transparent material for the same handedness of light with a small amount of reflection at the bottom layer and the intrinsic Ohmic loss of Al. As a result, the proposed stacked nano-grating structure can provide ultra-broadband circular polarization selectivity.

4.2.3 The helically stacked multiple nanograting layers

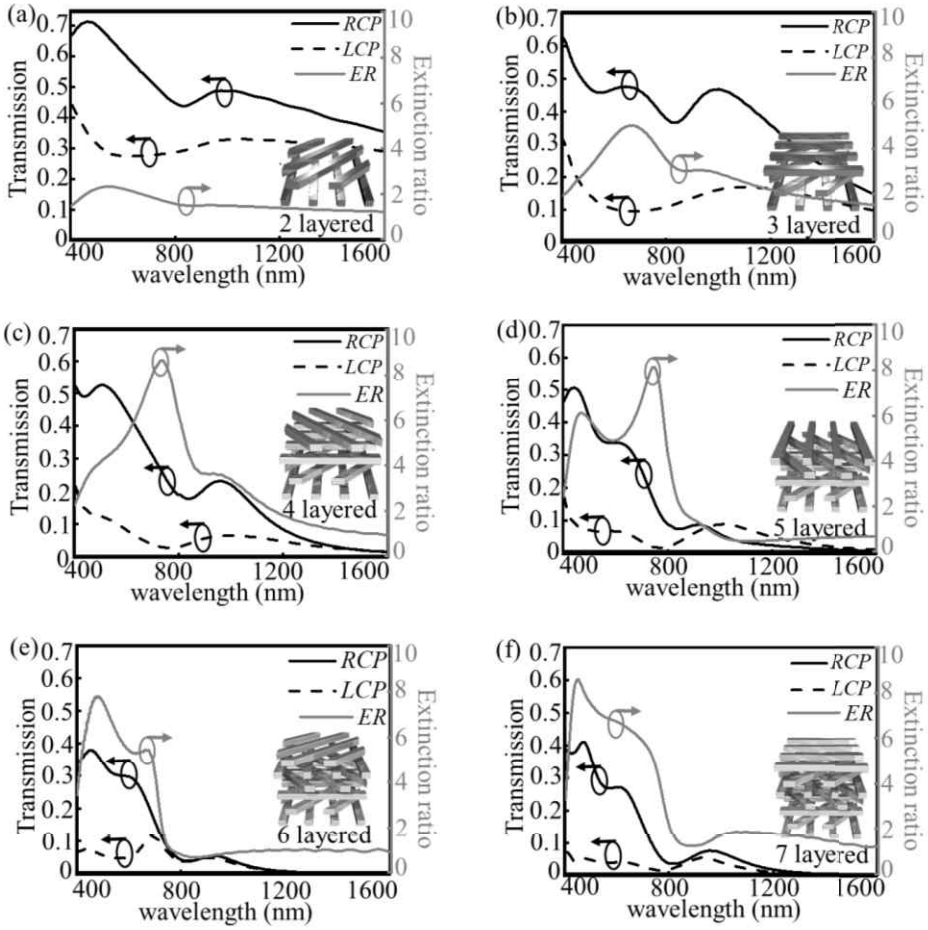

Figure 4.5 Transmission curves and *ER* for CP light as changing the number of the helically stacked nano-grating layers. The structures are constructed with left handed manner, and structure parameters are p = 150 nm, $w = t$ = 30 nm, d = 30 nm and θ = 45°.

The bianisotropic effect at the visible wavelength ranges of interest is investigated with the helically stacked multiple layers

as shown in Fig. 4.5. The more the nano-grating layers are helically stacked with the left handed configuration, the more the structures block LCP light over the wide wavelength range because they exhibit the longer 3D chiral current loops along with the stacked layers. In the case of RCP incident light, it remains nearly transparent. But the overall transmittance decreases due to the intrinsic loss of Al. This result is in a good agreement with the aforementioned results that the helically stacked nano-grating can pass the same handedness of light and reflect most of the opposite handedness one. As increasing the number of the nano-grating layers, the averaged *ER* of the seven-layered structure reaches up to ~8 over the entire visible wavelength regime. Note that the proposed design remains with subwavelength thickness of 390 nm even with seven layers of stacking, which corresponds to about one-tenth of the thickness required for conventional polymer based micro-circular polarizers. Therefore, the proposed helically stacked nano-grating structure can be a promising candidate as an ultrathin circular polarizer for visible wavelength range.

Figure 4.6 shows the transmission spectra of the 7-layered structures varying *d*. As *d* increases, the transmission band for RCP incident light shifts to a longer wavelength. This indicates that the spatial frequency of the helically stacked structures has to match that of the wavelength of the incident light.

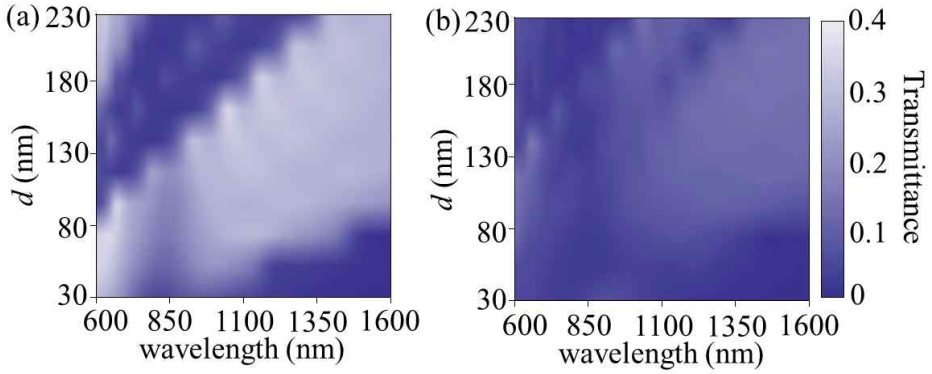

Figure 4.6 Transmission spectra of the 7-layered structures varying *d* for (a) RCP and (b) LCP incident light.

Next, to understand the physical effects of each geometrical parameter of the structure are investigated. For achieving high performance circular polarizer, it is needed to consider not only *ER* but also transmission of the selected polarization over the entire visible wavelength range. Also, the chiral effect in the helically stacked structures may be determined by twisted angle θ and the separation distance *d*. Therefore, averaged *ER* and averaged transmission for RCP incident light are calculated as changing θ and *d* (Figs. 4.7(a) and 4.7(b)). The averaged values are calculated over wavelength ranges from 400 nm to 700 nm.

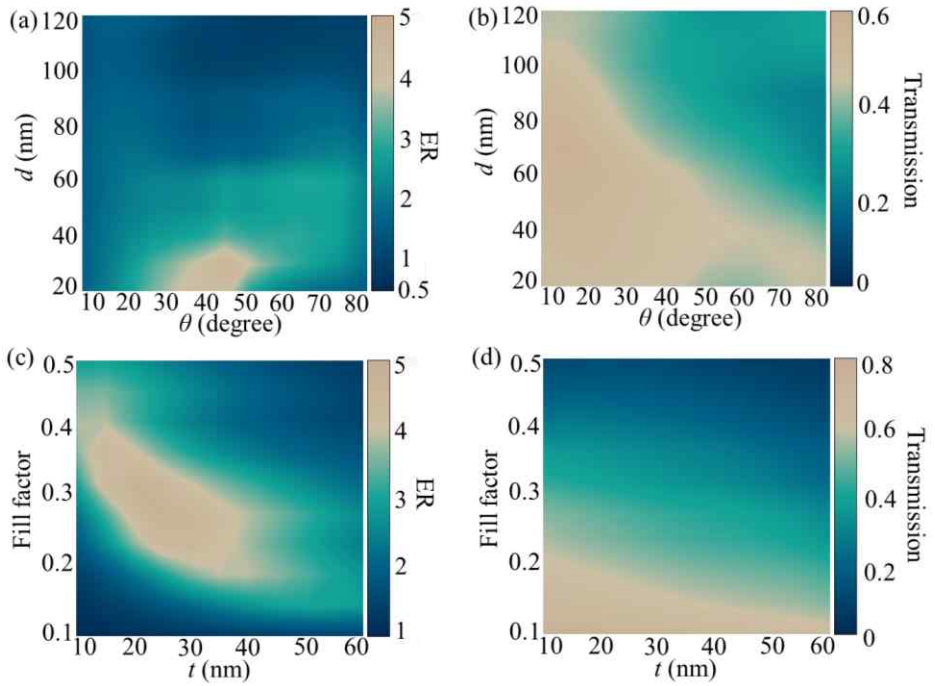

Figure 4.7 Averaged extinction ratio (T_{RCP}/T_{LCP}) and (b) averaged transmission for RCP light of the four-layered Al nano-grating structure over the wavelength ranges from 400 nm to 700 nm as a function of d and θ. (c) The averaged extinction ratio and (d) averaged transmission for RCP light of the four-layered Al nano-grating structure with fixed d = 30 nm and θ = 45° as a function of t and fill factor.

The nano-grating structures with small θ lead to low averaged ER because they form weak 3D chirality. Also, as can be seen, the averaged ER decrease when the distance d increases from 30 nm to 120 nm. This is because the 3D chiral current loop for LCP light is formed at larger wavelength as d becomes larger. Thus, d = 30 nm and θ = 45° are set to optimized values with the

highest averaged *ER* and moderate RCP transmission. In addition, as discussed above, the chirality of the proposed structures is resulted from stacking helically the anisotropic transmissive layers. Therefore, whether each nanograting layer can be regarded as transmissive current sheet having anisotropic current flows plays a significant role in the proposed structure. To investigate the physical effect of the geometrical parameters of the nanograting, the averaged *ER* and averaged transmission for RCP incident light are calculated as changing t and fill factor with fixed d = 30 nm and θ = 45° (Figs. 4.7(c) and 4.7(d)). The highest averaged *ER* can be obtained at fill factor of 0.2-0.3 and t of 20-30 nm, and the averaged transmission dramatically decreases when fill factor increases. Therefore, fill factor and t are set to 0.2 and 30 nm, respectively, for the high transmittance and fabrication feasibility of the nano-grating layer.

4.3 Experimental demonstrations

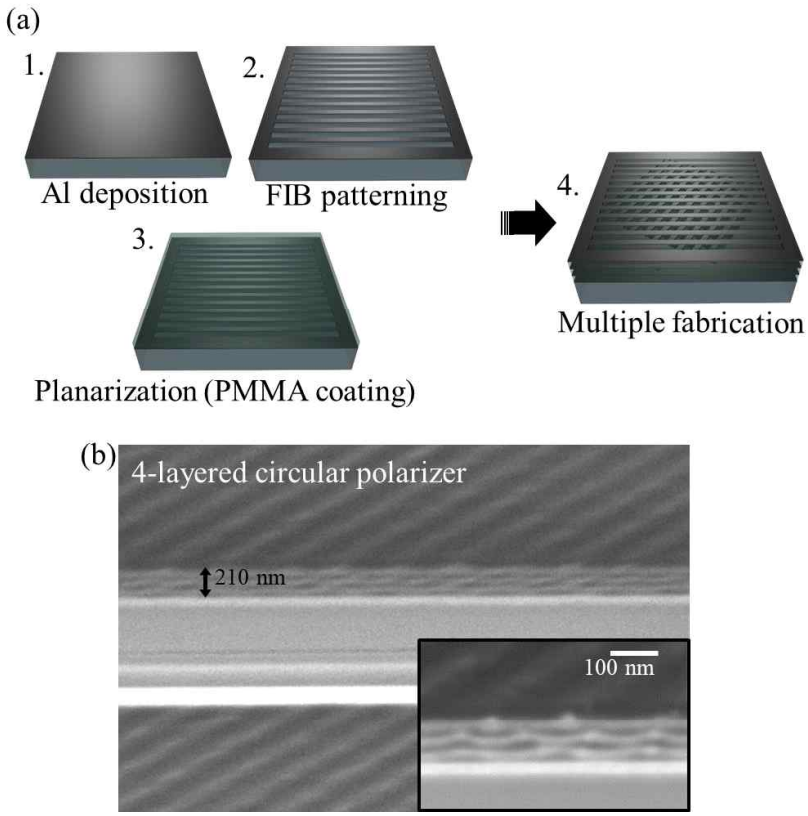

Figure 4.8 (a) Flow chart of the fabrication process for helically stacked nanograting layers. (b) Cross-sectional SEM images of the fabricated sample.

To experimental demonstration of the proposed structures, a prototype of the proposed structure is fabricated with p = 150 nm, w = t = 30 nm, d = 30 nm and θ = 45° in an area of 15 μm by 15 μm using successive focused ion beam (FIB) milling method based on the fabrication scheme described in Fig. 4.8(a). For the

fabrication of four-layered nano-grating structure, at first, 30-nm-thick Al layer is deposited on a glass substrate using electron beam evaporator (MUHAN, MHS-1800). Next, the nano-grating patterns are milled on the Al layer using focused ion beam milling machine (FEI, Quanta 200 3D), and then 30-nm-thickness polymethyl methacrylate (PMMA) is spin coated for planarization process. This process for the single nano-grating layer is conducted sequentially with twisted angle of 45° for the four-layered nano-grating based circular polarizer. Figure 4.8(b) shows a cross-sectional SEM image of the four-layered nano-grating structure. The structure is fabricated with the left handed manner (θ = 45°), and the uppermost layer forms an angle of 45° with respect to y-axis. For polarization sensitive optical measurement, CCD images of the transmitted light is captured under the incident light of the selected polarized light, LCP, and the unselected polarized light, RCP, at 532 nm, 660 nm and 980 nm (Fig. 4.9(a)). For the optical measurement, three different monochromatic continuous wave lasers with center wavelength of 532 nm, 660 nm and 980 nm were exploited as the input light. The input light sequentially passes through a quarter-wave plate, a half-wave plate, the four-layered nano-grating sample, an objective lens, a second quarter-wave plate and a linear polarizer, and then the output light is captured by CCD cameras.

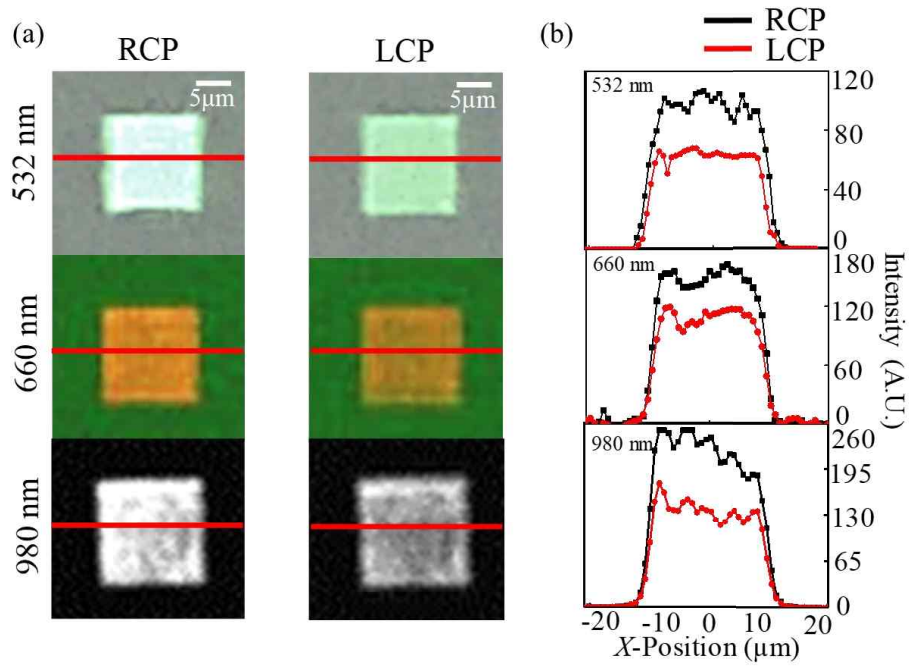

Figure 4.9 (a) The captured CCD images from the fabricated sample at 532 nm, 660 nm, and 980 nm. The left figure is for RCP incident light and the right one for LCP incident light. (b) The output intensity of the RCP light (black) and LCP light (red) along the red line in Fig. 4.8(a) is shown.

For *ER* calculation, the intensities of the CCD images are compared as shown in Fig. 4.9 (b). The *ER*s of 1.651, 1.479, and 1.821 are calculated at 532nm, 660nm and 980nm, respectively. It can be seen that the RCP incident light passes well through the fabricated structure while the LCP incident light passes through it with relatively low intensity. However, transmission for LCP incident light is not suppressed enough compared to the

simulation result (Fig. 4.5(c)). This is because the fabricated Al nano-gratings have blunt edges under the FIB milling process of nano-scale width and thickness less than 50 nm. Despite these imperfections in the fabricated structure, it is worth noticing that the proposed device and working principle present circular polarization selectivity in the full range of visible wavelengths for the first time

4.4 Discussion & Conclusion

4.4.1 For various optical systems

For the aforementioned sections, the ultrathin circular polarizer is focused on the broad bandwidth ranging from visible to near-infrared wavelengths. Actually, it can be required to revise the configuration and materials of the proposed structures, depending on the practical optical systems. For example, it is sufficient for the circular polarizer used for visible display systems to operate at moderate bandwidth covering from 380 nm to 750 nm. In this case, combination of resonant nanorod and non-resonant nanograting layer might provide better *ER* over the entire visible wavelengths. In addition, the proposed design can be extended to wider wavelength ranges when Al is replaced to other noble metals. For example, helically stacked gold or silver nano-gratings can be good ultra-broadband circular polarizers for near infrared wavelength ranges. The proposed helically stacked nano-grating design can be applied to micro circular polarizers operating in various wavelength range through scaling up the structure with different metals having low intrinsic loss. Here, transmission curves are calculated for the gold (Au) and silver (Ag) based cases with four-layered structure as shown in Fig. 4.10. In the proposed structure, cross-polarization components of transmission matrices for circularly polarized incident light are successfully suppressed, and thus the

transmitted wave is circularly polarized light. Unlike Al, Au and Ag do not have strong intrinsic losses in the near infrared wavelength range, so an ultra-broadband circular polarization selectivity can be obtained.

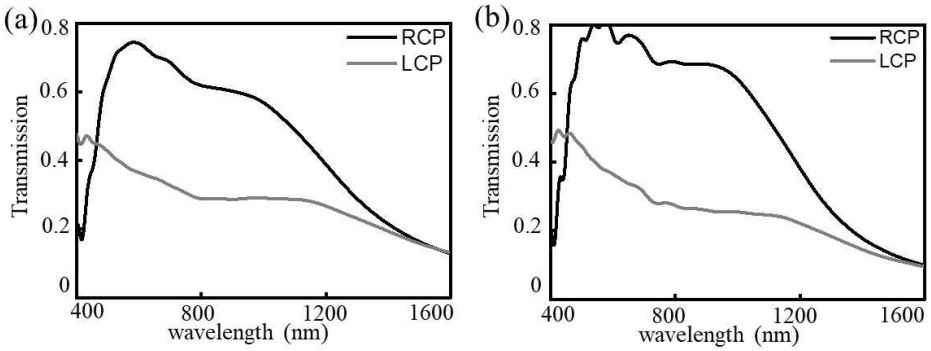

Figure 4.10 Transmission curves for (a) the helically stacked gold nano-grating and (b) the helically stacked silver nano-grating. The structures are helically stacked with the four layers of the nano-gratings as shown in the inset of Fig. 4.5(c), and the structure parameters are p = 150 nm, w = t = 30 nm, d = 30 nm and θ = 45°.

Therefore, it is important to re-optimize the configuration and materials of the structure to apply the proposed structures to various optical systems.

4.4.2 Conclusion

In this section, the concept of the helically stacked Al nano-grating structure which provides non-resonant characteristics of

circular polarizer for the visible light with ultra-thin thickness is demonstrated. The bianisotropic effect is obtained in a broad range of visible wavelengths and experimentally demonstrated. For the visible wavelength range, the non-resonant structure provides broader bandwidth and higher *ER* than resonance-based structure by overcoming the trade-off between bandwidth and *ER*. Also, the helically stacked Al nano-grating structure is highly suitable for practical applications in terms of cost and mass production, especially considering abundancy of Al in the earth crust and simple fabrication process. Furthermore, due to the simple structure of the nano-grating, nano-imprinting lithography method can be introduced to reduce cost with high throughput and resolution. Also, through scaling up the structures or using other materials [80] having low intrinsic absorption loss, it is easy to apply the proposed design to ultra-broadband strong biansiotropy effects in various wavelength ranges. Based on the proposed structure and methodology, it is possible to achieve extreme miniaturization of optical systems integrated with a circular polarizer such as polarization-resolved spectroscopies and mobile/wearable 3D displays.

Chapter 5. Conclusion

In this dissertation, novel optical devices using multi-layered metasurfaces are proposed to miniaturize various optical systems. The proposed structures are theoretically demonstrated and numerically verified. Also, some devices are experimentally testified their feasibility and performances. Here, the summary of the results of this dissertation is presented as followings.

In Chapter 2, the spatial modulator for amplitude and polarization rotation is realized by tri-layered anisotropic metasurfaces with thickness of 370 nm. The proposed structure allows the independent control of amplitude and the rotation angle of polarization plane of LP light. The proposed structure generates LP light with arbitrary rotation angle and amplitude modulation depth up to 0.9. Also, this independent control exhibits over broad wavelengths ranging from 700 nm to 1300 nm.

In Chapter 3, the meta-pixels that can provide graduation tuning of the expressed colors are demonstrated using the bi-layered hybrid metasurfaces with thickness of 470 nm. It is experimentally verified that the resonance wavelength and intensity of the transmitted light can be independently controlled by adjusting the sizes (length & width) and the rotated angle of the nanorods, respectively. Also, the highly saturated response colors originating from the cavity effect can be observed, and the structures express various colors varying from blue

to red. Furthermore, the meta-pixel that has orange and green as primary colors is experimentally described. The gradual tuning of response colors changing from orange to green is apparently seen in the meta-pixel samples. Therefore, the proposed meta-pixels could be a promising candidate for future displays such as AR, wearable, and foldable displays.

In Chapter 5, the ultrathin circular polarizer is demonstrated by the helically stacked nanogratings. The proposed circular polarizer has subwavelength thickness in spite of the multiple layers. The proposed structure can provide the operating bandwidth of 922 nm and the *FOM* of 1816, which are about 8 times larger than those of the helically stacked nanorod structure. Thus, it is verified that the proposed structures give a detour route for avoiding the trade-off relation between circular polarization selectivity and bandwidth. The proposed structure can provide the averaged extinction ratio up to 8 over entire visible wavelengths. In addition, the feasibility and the performance of the proposed structures are experimentally explained.

In the aforementioned sections, various novel optical devices are realized by the multi-layered metasurfaces. They can not only overcome the limitations of conventional optical components but also offer versatility by combining various optical functions within subwavelength thickness. Here, it is noticeable that the proposed devices are benefited from the insights that allow to intuitively predict the functions of the multi-layered structures in the role of the individual single layer metasurfaces. Due to these powerful advantages,

it is strongly expected that the proposed multi-layered metasurfaces can be applied to various next-generation optical devices.

Bibliography

1. J. Valentine, S. Zhang, T. Zentgraf, E. Ulin-Avila, D. A. Genov, G. Bartal, and X. Zhang, "Three-dimensional optical metamaterial with a negative refractive index", Nature **455**, 376–79 (2008).
2. N. Engheta, and R. W. Ziolkowski, *Metamaterials: Physics and Engineering Explorations* (Wiley & Sons, 2006)
3. D. Schurig *et al.*, "Metamaterial Electromagnetic Cloak at Microwave Frequencies". Science **314**, 977–80 (2006).
4. N. Yu, and F. Capasso, "Flat optics with designer metasurfaces". Nat. Mater. **13**, 139–150 (2006).
5. J. K. Gansel *et al.*, "Gold helix photonic metamaterial as broadband circular polarizer," Science **324**, 1513-1515 (2009).
6. Y. Zhao, M. A. Belkin, and A. Alù, "Twisted optical metamaterials for planarized ultrathin broadband circular pol

39. James, T. D., Mulvaney, P. & Roberts A. The plasmonic pixel: large area, wide gamut colour reproduction using aluminum nanostructures. Nano Lett. **16**, 3817-3823 (2016).
40. Coh, X. M. *et al.* Three-dimensional plasmonic stereoscopic prints in full colour. Nature Commun. **5**, 1-8 (2014).
41. Tan, S. J. *et al.* Plasmonic colour palettes for photorealistic printing with aluminum nanostructures. Nano Lett. **14**, 4023-4029 (2014).
42. Vashistha, V. *et al.* All-dielectric metasurfaces based on cross-shaped resonators for colour pixels with extended gamut. ACS Photonics **4**, 1076-1082 (2017).
43. Dong, Z. *et al.* Printing beyond sRGB colour gamut by mimicking silicon nanostructures in free-space. Nano Lett. **17**, 7620-7628 (2017).
44. Xiang, J. *et al.* Manipulating the Orientations of the Electric and Magnetic Dipoles Induced in Silicon Nanoparticles for Multicolour Display. Laser Photonics Rev. **12**, 1800032 (2018).
45. Flauraud, V., Reyes, M., Paniagua-Domínguez, R., Kuznetsov, A. I. & Brugger, J. Silicon nanostructures for bright field full colour prints. ACS Photonics **4**, 1913-1919 (2017).
46. Yang, C.-Y. *et al.* Nonradiating silicon nanoantenna metasurfaces as narrowband absorbers. ACS Photonics **5**, 2596-2601 (2018).
47. Kuznetsov, A. I., Miroshnichenko, A. E., Brongersma, M. L., Kivshar, Y. S. & Luk'yanchuk, B. Optically resonant dielectric nanostructures. Science **354**, aag2472 (2016).
48. Zhao, Q., Zhou, J., Zhang, F. & Lippens, D. Mie resonance-based dielectric metamaterials. Mater. Today **12**, 60-69 (2009).
49. Kristensen, A. *et al.* Plasmonic colour generation. Nature Rev. Mater. **2**, 16088 (2016).
50. Lee, T., Jang, J., Jeong, H. & Rho, J. Plasmonic- and dielectric-based structural colouring: from fundamentals to practical applications. Nano Convergence **5**(1), (2018).
51. Menzel, C. *et al.* Extreme coupling: A route towards local magnetic metamaterials. *Phys. Rev. B* **89**, 155125 (2014).
52. S.-J. Kim et al., Active directional switching of surface plasmon polaritons using a phase transition material. Sci. Rep. **7**, 43723 (2017).
53. C. Choi, S.-J. Kim, J.-G. Yun, J. Sung, S.-Y. Lee, and B. Lee, Deflection angle switching with a metasurface based on phase-change nanorods. Chin. Opt. Lett. **16**(5), 050009 (2018).
54. S.-Y. Lee *et al.*, Holographic image generation with a thin-film resonance caused by chalcogenide phase-change material. Sci. Rep. **7**, 41152 (2017).
55. T. Treibitz and Y. Y. Schechner, "Active polarization descattering," IEEE Trans. Pattern Anal. Mach. Intell. **31**, 385–399 (2009).
56. L. A. Nafie, "Circular polarization spectroscopy of chiral molecules," J. Mol. Struct. **347**, 83-100 (1995).
57. W.-L. Hsu, J. Davis, K. Balakrishnan, M. Ibn-Elhaj, S. Kroto, N. Brock, and S. Pau, "Polarization microscope using a near infrared full-Stokes imaging polarimeter," Opt. Express **23**, 4357-4368 (2015).
58. W. Sparks, J. H. Hough, T. A. Germer, F. Robb, and L. Kolokolova, "Remote sensing of chiral signatures on Mars," Planet. Space Sci. **72**, 111–115 (2012).

59. W. B. Sparks, J. H. Hough, L. Kolokolova, T. A. Germer, F. Chen, S. DasSarma, P. DasSarma, F. T. Robb, N. Manset, I. N. Reid, and F. D. Macchetto, "Circular polarization in scattered light as a possible biomarker," W. Martin, J. Quant. Spectrosc. Radiat. Transfer **110**, 1771–1779 (2009).
60. W. B. Sparks, J. Hough, T. A. Germer, F. Chen, S. DasSarma, P. DasSarma, F. T. Robb, N. Manset, L. Kolokolova, N. Reid, F. D. Macchetto, and W. Martin, "Detection of circular polarization in light scattered from photosynthetic microbes," Proc. Natl. Acad. Sci. U.S.A. **106**, 10871–10872 (2009).
61. A. B. Craig, Understanding Augmented Reality: Concepts and Applications (Boston, Elsevier, 2013).
62. J. Kaschke, L. Blume, L. Wu, M. Thiel, K. Bade, Z. Yang, and M. Wegener, "A helical metamaterial for broadband circular polarization conversion," Adv. Optical Mater. **3**, 1411–1417 (2015).
63. A. Kuzyk, R. Schreiber, Z. Fan, G. Pardatscher, E.-M. Roller, A. Hőgele, F. C. Simmel, A. O. Govorov, and T. Liedl, "DNA-based self-assembly of chiral plasmonic nanostructures with tailored optical response," Nature, **483**, 311-314 (2012).
64. M. Esposito, V. Tasco, F. Todisco, A. Benedetti, D. Sanvitto, and A. Passaseo, "Three dimensional chiral metamaterial nanospirals in the visible range by vertically compensated focused ion beam induced-deposition," Adv. Optical Mater. **2**, 154–161 (2014).
65. M. Esposito, V. Tasco, M. Cuscunà, F. Todisco, A. Benedetti, I. Tarantini, M. De Giorgi, D. Sanvitto, and A. Passaseo, "Nanoscale 3D chiral plasmonic helices with circular dichroism at visible frequencies," ACS Photonics **2**, 105–114 (2015).
66. J. H. Singh, G. Nair, A. Ghoshc, and A. Ghosh, "Wafer scale fabrication of porous three-dimensional plasmonic metamaterials for the visible region: chiral and beyond," Nanoscale **5**, 7224-7228 (2013).
67. G. K. Larsen, Y. He, J. Wang, and Y. Zhao, "Scalable fabrication of composite Ti/Ag plasmonic helices: controlling morphology and optical activity by tailoring material properties," Adv. Optical Mater. **2**, 245–249 (2014).
68. M. Esposito, V. Tasco, F. Todisco, M. Cuscunà, A. Benedetti, D. Sanvitto, and A. Passaseo, "Triple-helical nanowires by tomographic rotatory growth for chiral photonics," Nat. Commun. **6**, 6484 (2015).
69. Z. Li, H. Caglayan, E. Colak, J. Zhou, C. M. Soukoulis, and E. Ozbay, "Coupling effect between two adjacent chiral structure layers," Opt. Express **18**, 5375-5383 (2010).
70. L. Wu, Z. Y. Yang, Y. Cheng, Z. Lu, P. Zhang, M. Zhao, R. Gong, X. Yuan, Y. Zheng, and J. Duan, "Electromagnetic manifestation of chirality in layer-by-layer chiral metamaterials," Opt. Express **21**, 5239-5246 (2013).
71. Y. Zhao, M. A. Belkin, and A. Alù, "Twisted optical metamaterials for planarized ultrathin broadband circular polarizers," Nat. Commun. **3**, 870 (2012).
72. J. Liu, Z. Li, W. Liu, H. Cheng, S. Chen, and J. Tian, "High-efficiency mutual dual-band asymmetric transmission of circularly polarized waves with few-layer anisotropic metasurfaces," Adv. Optical Mater. **4**, 2028–2034 (2016).

73. C. Pfeiffer, C. Zhang, V. Ray, L. J. Guo, and A. Grbic, "High performance bianisotropic metasurfaces: asymmetric transmission of light," Phys. Rev. Lett. **113**, 023902 (2014).
74. R. Ji, S.-W. Wang, X. Liu, X. Chena, and W. Lu, "Broadband circular polarizers constructed using helix-like chiral metamaterials," Nanoscale **8**, 14725–14729 (2016).
75. W. Gao, H. M. Leung, Y. Li, H. Chen, and W. Y. Tam, "Circular dichroism in double-layer metallic crossed-gratings," J. Opt. **13**, 129501 (2011).
76. S. J. Tan, L. Zhang, D. Zhu, X. M. Goh, Y. M. Wang, K. Kumar, C.-W. Qiu, and J. K. W. Yang, "Plasmonic color palettes for photorealistic printing with aluminum nanostructures," Nano Lett. **14**, 4023–4029 (2014).
77. Y.-W. Huang, W. T. Chen, W.-Y. Tsai, P. C. Wu, C.-M. Wang, G. Sun, and D. P. Tsai, "Aluminum plasmonic multicolor meta-hologram," Nano Lett. **15**, 3122–3127 (2015).
78. B. Zheng, R. Zhang, M. Zhou, W. Zhang, S. Lin, Z. Ni, H. Wang, F. Yu, and H. Chen, "Broadband subwavelength imaging using non-resonant metamaterials," Appl. Phys. Lett. **104**, 073502 (2014).
79. T. J. Cui, D. R. Smith, and R. Liu, *Metamaterials: Theory, Design, and Applications* (Springer, 2010).
80. D. Neshev, and I. Aharonovich, "Optical metasurfaces: new generation building blocks for multi-functional optics," Light Sci. Appl. **7**, 58 (2018).

Appendix

Some portions of the work in this dissertation are also presented in the following publications:

Chapter 2:

J.-G. Yun, J. Sung, S.-J. Kim, and B. Lee, “Simultaneous control of polarization and amplitude over broad bandwidth using multi-layered anisotropic metasurfaces,” Optics Express, vol. 26, no. 23, pp. 29826-29836, 2018.

Chapter 5:

J.-G. Yun, S.-J. Kim, H. Yun, K. Lee, J. Sung, J. Kim, Y. Lee, and B. Lee, "Broadband ultrathin circular polarizer at visible and near-infrared wavelengths using a non-resonant characteristic in helically stacked nano-gratings," Optics Express, vol. 25, no. 13, pp. 14260-14269, 2017.

초 록

인공지능과 정보화 기술의 발전은 과학기술을 언제 어디서나 접근 가능하도록 만들고 있다. 이런 추세에 따라, 최신 정보화 기기들은 다양한 기술들을 융합하여 개발되고있으며 여러 복잡하고 다양한 기기들의 집적화를 통하여 제작된다. 하지만 기존의 광학 소자들은 두꺼운 부피를 가질 뿐만 아니라 집적화에 어려움 때문에 초소형 광학 소자 개발에 병목현상이 되고있다.

이러한 기존의 광학 소자의 한계점을 극복하기 위해서, 메타물질 및 메타표면을 이용한 초소형 광학 소자 개발이 활발히 연구되고있다. 하지만 메타표면은 빛과 물질의 상호작용이 약하고, 공정법이 제한적이고 복잡하여 실용화가 어렵기 때문에 초소형 광소자를 개발하는데 어려움을 겪고 있다.

본 박사학위 논문에서는 다양한 초소형 광학 소자들을 적층형 메타표면을 이용하여 개발하는 것을 목표로 한다. 적층형 메타표면은 여러 개의 메타표면을 파장이하의 간격을 두고 적층한 형태를 말한다. 이런 적층형 메타표면은 단일 메타표면과 비교하여 강한 빛과 구조의 상호작용을 유도할 수 있으며, 빛을 제어함에 있어서 높은 자유도를 갖기 때문에 다기능성 광학소자 개발에 유리하다. 또한, 3차원 메타물질에 비하여 공정 방법이 쉽고 기존의 반도체 공정을 이용할 수 있어 상용화 가능한 응용 소자를 제작하는데 용이하다. 본 박사학위 논문에서는 편광자와 같은 개별 광학 소자 뿐만 아니라 여러 광학 소자의 역할이 결합된 초소형 광학 소자를 개발한다.

첫째로, 투과 광의 진폭과 편광 회전을 독립적으로 조절 가능한 광학 소자를 제안한다. 제안된 소자의 구조는, 축의 회전 각도에 따라 빛의 편광을 회전시키는 역할을 하는 비등방성 나노막대와, 선형 편광자 역할을 하는 금속 격자구조가 회전하며 적층되어있는 구조이다. 투과광의 편광 회전 각도는 금속 격자구조의 회전각에 의하여 결정되며, 최종 투과율은 나노막대의 각도를 조절하여 결정된다. 따라서, 제안된 구조는 편광되지 않은 빛이 입사할 때, 임의의 편광 각도와 진

폭을 갖는 선형편광을 투과시킨다. 제안된 구조는 편광 회전자와 진폭 변조기의 기능을 수백 나노미터의 두께에서 구현이 가능하여 다양한 광소자에 적용 가능할 것이라 기대된다.

두번째로, 투과광의 파장과 세기가 독립적으로 제어가능하고, 넓은 색영역이 표현 가능한 초소형 컬러 픽셀을 제안한다. 제안된 구조는 액정표시장치에서 편광자, 컬러필터, 액정이 결합된 구조로 이해할 수 있다. 제안된 구조는 높은 굴절률의 나노막대 메타표면 위에 금속 격자구조 메타표면이 적층된 구조이며, 나노막대는 Mie 공진을 이용하여 특정 공진 파장에서만 편광 회전자로 동작한다. 이때, 공진 파장은 나노막대의 크기에 따라 결정되고, 회전자로의 동작 정도는 나노막대의 회전각에 의존한다. 따라서 제안된 적층형 구조에서, 최상층의 나노격자구조의 격자 축에 평행하게 편광된 백색광을 입사시키면, 나노막대와 격자구조 층간의 상호작용을 통하여 회전된 빛만이 투과되어 색이 결정된다. 또한, 제안된 구조를 이용하여 높은 색심도를 갖는 초소형 픽셀 구현 방법을 제안하였다. 제안된 구조는 얇은 두께와 초소형의 픽셀 크기에 장점이 있어 차세대 디스플레이 소자에 응용 가능할 것이라 기대된다.

마지막으로, 전체 가시광선 대역에서 동작 가능한 원형편광자를 금속 격자구조의 비공진적 특성을 이용하여 구현하였다. 제안된 구조는 금소 나노격자구조가 나선형으로 적층된 구조로, 구조의 회전 반향과 반대로 회전하는 광은 투과시키고 같은 방향으로 회전하는 광은 반사시키는 원리를 이용한다. 이때, 나노격자구조는 격자구조를 따라서 유도 전류를 비공진적으로 유도하여 광대역에 동작 가능하도록 만든다. 얇은 두께의 제안된 구조는 기존의 두꺼운 원형편광자를 대체하여 다양한 광학기기의 소형화에 도움이 될 것이라 기대된다.

본 박사학위 논문은 개별 광학소자 및 다기능이 결합된 광학 소자를 개발하여, 기존의 광학소자의 초소형화에 기여할 수 있을 뿐만 아니라 높은 자유도를 제공하여 새로운 광학소자 개발에도 활용될 수 있을 것이라 기대된다.

주요어: 메타표면, 적층형 구조, 진폭 변조기, 박막형 디스플레이, 편광 조절장치, 파장이하 두께 구조.
학 번: 2015-30199